ACCSCIENCE PUBLISHING

International Journal of Bioprinting

RESEARCH ARTICLE

# Immunomodulation and bone repair of 3D-printed SrBG/PCL scaffolds with PDA coating

**Qiping Huang[1,2†], Xiang Li[1†], Qinghong Fan[1†], Qian Du[1], Guangquan Zhao[1,2], Yuanhao Lv[1,2], Yixiao Wang[1], Weikang Xu[2,3,4*], and Qingde Wa[1*]**

[1]Department of Orthopedic Surgery, The Second Affiliated Hospital of Zunyi Medical University, Zunyi, Guizhou, China

[2]Institute of Biological and Medical Engineering, Guangdong Academy of Sciences, Guangdong Chinese Medicine Intelligent Diagnosis and Treatment Engineering Technology Research Center, Guangzhou, Guangdong, China

[3]Guangdong Provincial Key Laboratory of Medical Electronic Instruments and Materials, Guangdong Institute of Medical Instruments, Guangzhou, Guangdong, China

[4]National Engineering Research Center for Healthcare Devices, Guangdong Institute of Medical Instruments, Guangzhou, Guangdong, China

[†]These authors contributed equally to this work.

***Corresponding authors:**
Weikang Xu
(759200816@qq.com)

Qingde Wa
(wqd887zsy@126.com)

**Citation:** Huang Q, Li X, Fan Q, *et al.* Immunomodulation and bone repair of 3D-printed SrBG/PCL scaffolds with PDA coating. *Int J Bioprint.* 2025;11(4):350-377. doi: 10.36922/IJB025210211

**Received:** March 4, 2025
**Revised:** May 21, 2025
**Accepted:** June 5, 2025
**Published online:** June 6, 2025

**Copyright:** © 2025 Author(s). This is an Open Access article distributed under the terms of the Creative Commons Attribution License, permitting distribution, and reproduction in any medium, provided the original work is properly cited.

**Publisher's Note:** AccScience Publishing remains neutral with regard to jurisdictional claims in published maps and institutional affiliations.

## Abstract

3D-printed polycaprolactone (PCL) scaffolds are widely used for bone tissue engineering but suffer from deficiencies, such as difficulty in cell adhesion, lack of osteogenic activity, and poor immunomodulatory capacity. Enhancing the biological responsiveness of PCL scaffolds remains a key focus in bone tissue engineering. In this study, the following three types of scaffolds were prepared: (i) PCL, (ii) strontium (Sr)-doped bioactive glass (SrBG)/PCL, and (iii) polydopamine (PDA)/SrBG/PCL. The scaffolds were assayed *in vitro* for their effect on the expression of osteoinductive differentiation markers (ALP, RUNX2, and COL1), and their influence on macrophage (MP) (CD206, ARG, TNF-α, IL1β, IL-10, and IL-12) behavior was evaluated. Their effect on bone defect repair was assessed *in vivo* using micro-computed tomography (micro-CT), hematoxylin and eosin (HE) staining, Masson staining, and immunofluorescence staining (iNOS, CD163, BMP-2, and VEGF). The results demonstrated that PDA/SrBG/PCL scaffolds significantly promoted the proliferation and osteogenic differentiation of bone marrow mesenchymal stem cells (BMSCs), inhibited the differentiation of MPs to the M1 phenotype, and promoted the differentiation of MPs to the M2 phenotype, resulting in better pro-osteogenic, immunomodulatory, and angiogenic effects *in vivo*. This observation may be associated with the release of $Sr^{2+}$ from SrBG, and surface modification with PDA further enhanced the immunomodulation and bone repair ability of the scaffold. The study demonstrated that the PDA/SrBG/PCL scaffolds exhibit excellent bone repair capabilities and hold strong potential for applications in bone tissue engineering.

***Keywords*:** 3D printing; Bone repair; Immunomodulation; Polycaprolactone; Polydopamine; Strontium-doped bioglass

## 1. Introduction

Bone defects refer to the destruction of bone tissue caused by trauma, infection, tumors, or other pathological conditions.[1] Tissue engineering is a promising strategy for reconstructing bone defects, and it has received much attention recently. To enhance repair effectiveness, many past studies have explored the composition, degradation properties, and bone-regenerative properties of composite scaffolds.[2–4] Although the mechanical properties and degradation characteristics of scaffolds have significantly improved, bone repair results remain unsatisfactory, limiting their clinical application.[5,6] In addition, scaffold–tissue interactions play a central role in tissue repair.[7] Therefore, elucidating and modulating scaffold–tissue interactions is essential to improve repair outcomes. Recent studies have found that bone filler materials trigger innate and adaptive immune responses after implantation.[8,9] Excessive immune responses may lead to chronic inflammation, fibrosis, and implant failure, increasing the risk of secondary surgery.[10–12] Therefore, reducing inappropriate immune responses triggered during early implant stages is particularly important. Macrophages (MPs) play a key immunoregulatory role in bone defect repair, with M1 (pro-inflammatory) and M2 (anti-inflammatory) MPs regulating bone formation, remodeling, and repair by secreting different cytokines.[13,14]

Biodegradable polymers create favorable conditions for regenerating new bone tissue and defect repair compared to permanent implants.[15] In comparison with inorganic materials, polymer materials have better degradability, higher biocompatibility, and more stable mechanical properties.[16,17] Among various degradable materials, synthetic polyesters have controlled biodegradability *in vivo* and are non-toxic.[18] Synthetic polyester-based materials have better mechanical properties than natural polymers and are more suitable for bone repair.[19] Among them, polycaprolactone (PCL) has good biocompatibility and can be effectively combined with biological tissues.[20,21] However, PCL has low bioactivity, poor cell adhesion, and lacks osteogenic activity.[22,23] In addition, Tang et al.[24] prepared *Panax notoginseng* saponin (PNS)-PCL scaffolds via 3D printing to evaluate their reparative effect on vascular injury in rabbit carotid arteries, and the inflammation scoring results indicated that pure PCL scaffolds exhibited poor anti-inflammatory performance. Therefore, PCL needs to be compounded with other biomaterials to enhance its osteogenic activity and immunomodulatory ability.

Bioactive glass (BG) is an inorganic bioactive material that can form strong bonds with hard and soft tissues, and it is widely used in bone tissue engineering due to its excellent biocompatibility, degradability, and bone-enhancing properties.[25] Research has demonstrated that mesoporous BG (MBG) effectively enhances apatite production rate.[26] Zhao et al.[27] used an MBG composite fibrin hydrogel for maxillofacial bone defect implantation, and MBG enhanced the mechanical strength, bioactivity, and osteogenic properties of the hydrogel. In addition, BG exhibits excellent cytocompatibility and antimicrobial effects as a coating material for metal implants.[28,29] In contrast, recent studies have reported that exosomes generated from MBG-stimulated mesenchymal stem cells (MSCs) are significantly more productive and exhibit enhanced immunomodulatory and bone repair capabilities.[30] In recent years, strontium-doped BG (SrBG) has received attention for its ability to promote osteoblast proliferation, osteogenic differentiation, and angiogenesis.[31] $Sr^{2+}$ inhibits the expression of inflammatory genes and provides a favorable environment for tissue repair.[32] In addition, $Sr^{2+}$ has immunomodulatory effects and is concentration-dependent.[33] Ding et al.[34] found that SrBG was able to mobilize monocytes from the spleen to reach the bone defect site and convert them into M2 MPs to promote bone tissue regeneration. SrBG promotes bone repair by activating the Akt signaling pathway to promote M2 MP polarization and release osteogenesis-related cytokines.[35] Although PCL/SrBG composite scaffolds displayed better bioactivity and osteogenic induction compared to PCL scaffolds, PCL/SrBG scaffolds alone were still insufficient to induce significant osteogenic differentiation.[36,37] Poh et al.[38] cultured PCL and PCL/SrBG scaffolds under non-osteoinductive conditions to evaluate their positive effect on osteoinductive differentiation; the PCL/SrBG scaffolds did not exhibit any significant osteoinductive differentiation ability, which may be related to the concentration of $Sr^{2+}$ released by the scaffolds. Polydopamine (PDA) is an implant surface modification material with good hydrophilicity, biocompatibility, antimicrobial properties, and bone-enhancing properties.[39] More importantly, the PDA coating has a large number of catecholamine groups for scavenging reactive oxygen species (ROS) and anti-inflammatory properties that inhibit M1 MP polarization and activate MP polarization toward the M2 phenotype, thereby promoting the expression of osteogenesis-related cytokines.[40] Jin et al.[41] demonstrated that PDA inhibits pro-inflammatory cytokine expression in MPs by downregulating the TLR-4-MYD88-NF-κB pathway. Moreover, PDA can regulate ROS production and upregulate heme oxygenase 1 (HO-1) expression, thereby influencing MP phenotypic differentiation and suppressing the inflammatory response. In this study, we innovatively and synergistically used PDA and SrBG to modify the surface and interior of PCL scaffolds to enhance the cell adhesion and proliferation of the scaffolds.[42] PDA coating

can better regulate the concentration of $Sr^{2+}$ released from the scaffold, helping to modulate the immune microenvironment and promote bone regeneration.

Briefly, we used PCL scaffolds as the basis for constructing PDA/SrBG/PCL composite scaffolds (Figure 1). These were prepared by loading SrBG, followed by surface modification with PDA. The study systematically evaluated the physical properties, biocompatibility, osteogenic differentiation, and immunomodulation of PCL, SrBG/PCL, and PDA/SrBG/PCL scaffolds to optimize new bone defect repair materials.

## 2. Materials and methods

### 2.1. Materials

Ethyl orthosilicate (TEOS), cyclohexane, triethyl phosphate (TEP), calcium nitrate tetrahydrate (CN), strontium nitrate, sodium hydroxide, anhydrous ethanol, and methylene chloride were purchased from Guangzhou Chemical Reagent Factory (China). Dodecyl amine (DDA) was purchased from Shanghai Aladdin Reagents Co. (China). Deionized water was purchased from Merck Millipore (Germany). PCL (molecular weight: 54,000) was purchased from Jinan Dai Gang Biotechnology Co. (China). Vitamin C and sodium β-glycerophosphate were purchased from Shanghai McLean Biochemical Technology Co., Ltd. (China). Dexamethasone was purchased from J&K Scientific (China). Hipure RNA kit, HiFiScript cDNA synthesis kit, and Ultra SYBR mixture (low ROX) were purchased from CWBIO (China). Alkaline phosphatase (ALP) kit, BCA protein assay kit, and RIPA lysate were provided by Bi Yun Tian Biotechnology (China). Dulbecco's modified Eagle's medium (DMEM), fetal serum, penicillin-streptomycin solution, phosphate buffer, trypsin, and CCK-8 kit were provided by ATCC (United States of America [USA]). Rat bone marrow MSCs (BMSCs) and MPs (RAW264.7) were provided by ATCC (USA). PDA was purchased from Tangshan Wei Hao Co.,

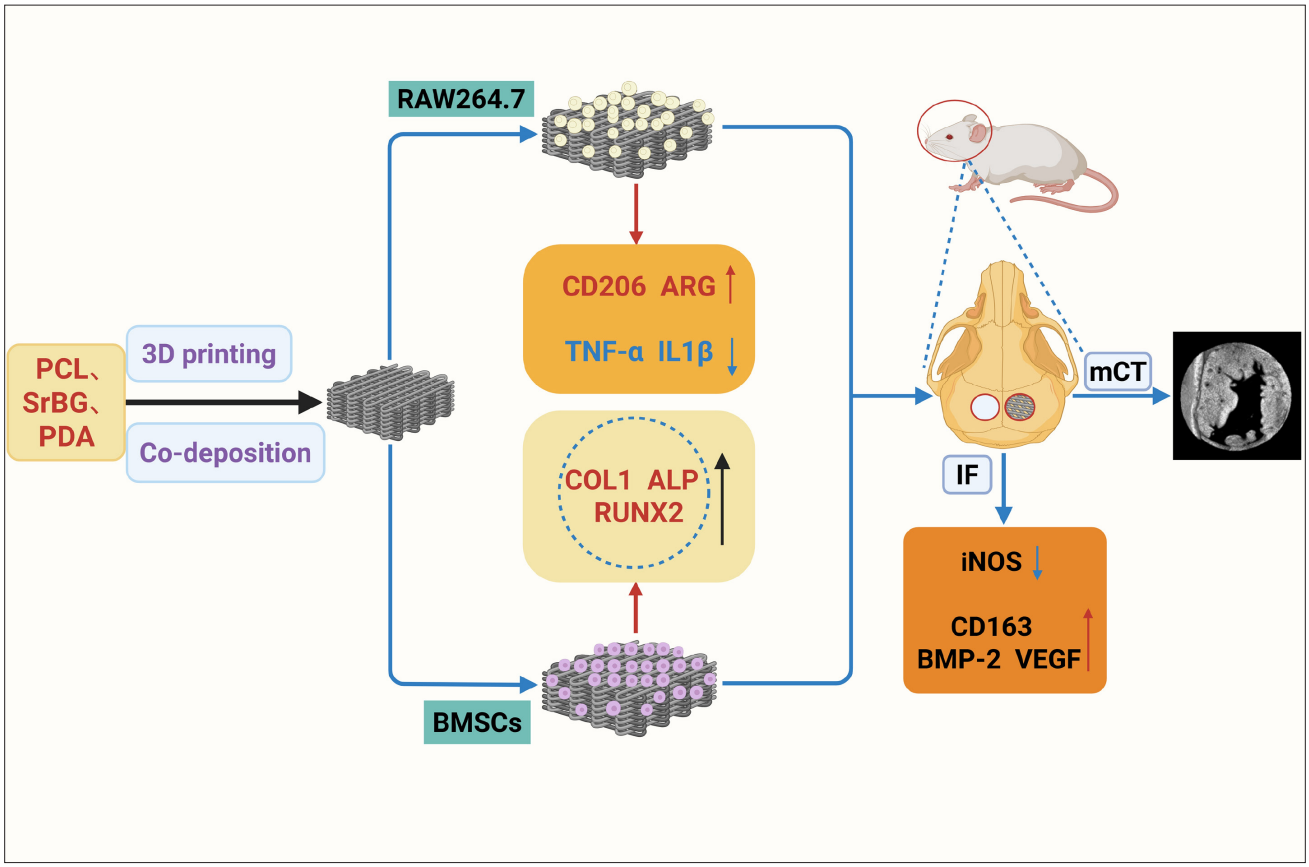


**Figure 1.** Schematic diagram of the development and systematic assessment of various PCL scaffolds. Abbreviations: ALP, alkaline phosphatase; ARG, arginase; BMP-2, bone morphogenetic protein-2; BMSCs, bone marrow mesenchymal stem cells; CD163, hemoglobin scavenger receptor; CD206, cluster of differentiation 206 (mannose receptor); COL1, Type I collagen; IF, immunofluorescence; IL, interleukin; INOS, inducible nitric oxide synthase; mCT, micro-CT; Runx2, Runt-related transcription factor 2; TNF-a, tumor necrosis factor-α; PCL, polycaprolactone; PDA, polydopamine; SrBG, strontium substituted bioactive glasses; VEGF, vascular endothelial growth factor.

Ltd. (China). Sprague-Dawley (SD) rats were provided by Chongqing Teng Xin Hua Fu Laboratory Animal Sales Co, Ltd. (China) (animal qualification certificate no. SYXK [Qian] 2021-0003).

### 2.2. Preparation of PCL, SrBG/PCL, and PDA/SrBG/PCL scaffolds

#### *2.2.1. Preparation of SrBG*

The molar ratio of the components of SrBG was designed as 60 $SiO_2$:30 CaO:6 SrO:4 $P_2O_5$. The specific experimental method for the preparation of micro- and nano-SrBG microspheres using the sol–gel method is described below.

The experimental temperature was maintained at 40°C using a water bath, and 5 g of DDA was fully dissolved in a mixture of deionized water and anhydrous ethanol. After that, 16.5 mL of TEOS and TEP was sequentially added to the solution using a syringe pump at a speed of 0.5 mL/min. CN and strontium nitrate were then added slowly, and the solution was stirred continuously for 3 h. Thereafter, the solution was kept at room temperature for 24 h to obtain a glass sol, which was subsequently washed and centrifuged to obtain a white precipitate. The precipitate was pre-frozen in the refrigerator at –20°C for 2 h and then freeze-dried. Finally, the freeze-dried precipitate was heated in a muffle furnace at 650°C for 3 h to obtain the SrBG, which was dried and stored after ball milling and sieving.

#### *2.2.2. Preparation of SrBG/PCL scaffolds*

Approximately 100 mg of SrBG powder was dispersed in 10 mL of dichloromethane solution containing 1 g PCL. After stirring, the solution was poured into glass dishes, and the dichloromethane was fully evaporated to obtain the scaffold raw material SrBG/PCL. The SrBG/PCL was transferred to the 3D printer (EFL-BP-6603, Suzhou Institute of Intelligent Manufacturing, China), and the printing parameters were set as: diameter: 5 mm, number of layers: 5 layers, layer thickness: 0.2 mm, infill density: 75%, barrel temperature: 65°C, and nozzle temperature: 70°C. The SrBG/PCL was heated, melted, and subsequently printed into cylindrical 3D scaffolds (diameter: 5 mm; height: 1 mm), referred to as the SBP group. For comparison, PCL was directly loaded into the 3D printer to fabricate a cylindrical 3D scaffold, designated as group P.

#### *2.2.3. Preparation of PDA/SrBG/PCL scaffolds*

The SrBG/PCL scaffolds were then modified using PDA. A Tris–HCl buffer (pH 8.5) was first prepared using 1.21 g Tris-base and 100 mL deionized water, and it was then stored at room temperature until further use. Thereafter, approximately 0.25 g dopamine hydrochloride (2.5 g/L) was added to the Tris–HCl buffer and stirred. The ready-to-use solution was stored in the dark until further use. At room temperature, the 3D-printed SrBG/PCL scaffolds were soaked in the weakly basic dopamine solution and shaken at 30°C on a shaking bed for 6 h. The SrBG/PCL scaffolds were then washed with deionized water to remove unattached polydopamine and dried to obtain the PDA/SrBG/PCL scaffolds (referred to as the PSBP group).

### 2.3. Scaffold characterization

#### *2.3.1. Morphology of SrBG*

The micromorphology of SrBG was characterized using a field emission scanning electron microscope (SEM) (Merlin, Germany); the particle size distribution of SrBG was analyzed using dynamic light scattering (DLS) (Malvern Panalytical, England).

#### *2.3.2. Surface morphology of the scaffolds*

The surface morphology and structure of the P, SBP, and PSBP scaffolds were observed using SEM (Merlin, Germany) at an accelerating voltage of 10 kV after gold-spraying the surface of the scaffolds. The average pore area of the scaffold fiber surface was statistically analyzed using ImageJ software.

#### *2.3.3. Hydrophilicity of the scaffolds*

The scaffolds were placed on a contact angle tester (c, KRUSS, Germany), and a 2-μL droplet was placed on the surface of the scaffolds. The position of the sample in contact with the droplet was adjusted to align with the baseline of the measurement; photographs were taken to obtain a still image of the droplet, and the magnitude of the contact angle ($\theta$) was calculated using contact angle measurement software DSA25 for each scaffold group.

#### *2.3.4. Porosity of the scaffolds*

The mass of the dried scaffold sample (M0), the total mass of the specific gravity bottle containing anhydrous ethanol at room temperature (M1), the total mass of the bottle and sample after sonication for 10 min to remove air bubbles (M2), and the remaining mass after the sample was removed (M3) were measured accordingly. The porosity of the obtained scaffolds was calculated using **Equation (I)**:

$$\text{Porosity} = \frac{M2 - M3 - M0}{M1 - M3} \quad \text{(I)}$$

#### *2.3.5. Ion release profile of the scaffolds*

Each scaffold (approximately 20 mg) was immersed in 5 mL phosphate-buffered saline (PBS) and shaken at 37°C and 60 rpm. Samples were collected on days 1 and 3, and the concentration of $Sr^{2+}$ was measured using the

inductively coupled plasma optical emission spectrometer (ICP-OES) (Agilent 5110, Agilent Technologies, America).

#### 2.3.6. Thermodynamic analysis of the scaffolds

The thermal weight loss data of the scaffolds were determined using a thermogravimetric analyzer (NETZSCH, Germany), in which the samples were heated from room temperature to 800°C at a rate of 10°C/min in a nitrogen atmosphere.

#### 2.3.7. Mechanical strength of the scaffolds

The mechanical properties of the scaffolds were analyzed by placing the scaffolds on an INSTRON tester (34 sc-5, Instron, America), drying them, and compressing them at a rate of 1 mm/min.

### 2.4. *In vitro* experiments

#### 2.4.1. Cell culture and scaffold sterilization

The BMSCs and RAW264.7 cells were cultured in a cell culture incubator (MCO-18AIC, PHC, Japan) at 37°C and 5% $CO_2$. The basal medium used was high glucose medium (DMEM), supplemented with 10% fetal bovine serum (FBS), 100 μg/mL penicillin, and 100 μg/mL streptomycin. During culture, the medium was changed daily or every 2 days, depending on the cell condition. Cells were passaged upon reaching 70–80% confluency, and only cells from passages 3 to 5 were used. Before the experiment, each group of scaffolds was immersed in a 75% ethanol solution for 2 h; the scaffolds were rinsed three times and stored overnight in PBS inside an ultraviolet (UV) sterilizer (30–800 L, Sheng Zhi Yuan and Science and Education Equipment Co., China).

#### 2.4.2. Cell activity assay

After BMSCs adhered and proliferated on the scaffold surface for 3 days, the morphology and distribution of cells on the scaffold surface were observed by staining the cells on the scaffold surface with a live-dead cell dye. The morphology and distribution of cells on the scaffold surface were observed using an inverted fluorescence microscope (Leica Microsystems, Germany).

#### 2.4.3. Histocompatibility assessment

Rat bone marrow MSCs (BMSCs) were utilized to evaluate the histocompatibility of different cells with the scaffolds. Briefly, sterile scaffold samples were placed in 48-well plates, and the samples were inoculated with $5 \times 10^4$ BMSCs. The supernatant was aspirated after 1, 3, and 7 days of incubation, and the rate of cell proliferation on the different scaffolds was assessed using the CCK-8 kit assay, which was performed using an enzyme marker (Tecan Spark, Austria) to measure the absorbance (optical density [OD]) at 450 nm.

#### 2.4.4. ALP staining and activity analysis

The scaffolds and BMSCs of each group were cultured with an osteogenic induction solution. After 7 days of culture, ALP dye was added to stain the samples, and the absorbance (OD) at 405 nm was measured by an enzyme marker. The cellular activity of the composite scaffold group relative to the control group was calculated from the measured OD values. The ALP-stained cells on the scaffold surface were observed using an inverted fluorescence microscope (Leica Microsystems, Germany).

#### 2.4.5. In vitro osteogenic capacity

Approximately $1 \times 10^5$ BMSCs were added to 48-well plates containing the scaffold samples. After 24 h of incubation, the supernatant was aspirated and discarded. Complete medium, osteogenic induction medium (100 mL complete medium + 0.39 mg dexamethasone + 1.76 mg vitamin C + 306.11 mg sodium β-glycerophosphate), or MP-conditioned medium was added, respectively; the culture medium was changed regularly. After 7 and 14 days of osteogenic induction, the expression of osteogenic marker genes of ALP (*ALP*), Runt-associated transcription factor 2 (*RUNX2*), and collagen type I (*COL1*) was measured using real-time fluorescence quantitative polymerase chain reaction (qRT-PCR). *GAPDH* was used as the internal reference gene. ALP activity was measured on days 7 and 14 using the ALP kit combined with the BCA method.

#### 2.4.6. MP polarization gene expression levels

RAW264.7 cells were inoculated into the scaffold samples and transferred to 48-well plates at a density of $5 \times 10^4$ cells per well. The complete medium was changed every 2–3 days. The medium removed from each set of samples was collected and mixed with osteogenic induction solution at a ratio of 1:5 to prepare MP-conditioned medium for backup. The expression of the M1 MP immune marker genes, including tumor necrosis factor-α (*TNF-α*) and recombinant human interleukin 1β (*IL1β*), and the M2 MP immune marker genes, including CD206 (*CD206*) and arginase (*ARG*), were detected using qRT-PCR on days 1 and 3. *GAPDH* was used as the internal reference gene. As shown in Table 1, the base sequences of each gene are presented.

#### 2.4.7. ELISA assay

The concentrated washing solution (phosphate buffer [PBS] containing Tween-20, with a pH value of 7.2–7.4.) was heated in a water bath to dissolve the crystals completely. The concentrated washing solution was diluted with distilled water at a 1:20 ratio. Substrate solutions A (chromogenic reagent A, hydrogen peroxide) and B (chromogenic reagent B, tetramethylbenzidine) were mixed thoroughly in a 1:1 volume ratio and used within 15 min after mixing. All reagents, including standards,

**Table 1. Specific primers for immunoregulatory and osteogenesis-related genes**

| Gene | Primer sequence (5'–3') | |
|---|---|---|
| | Forward | Reverse |
| *TNF-α* | GGGTGTTCATCCATTCTC | GGTCACTGTCCCAGCAT |
| *IL1β* | TACAGGCTCCGAGATGAACA | AGGCCACAGGTATTTTGTCG |
| *ARG* | CATATCTGCCAAAGACATCG | GGTCTCTTCCATCACCTTGC |
| *CD206* | ATGGATGTTGATGGCTACTGG | TTCTGACTCTGGACACTTGC |
| *ALP* | GGAGATGGTATGGGCGTCTC | GGACCTGAGCGTTGGTGTTA |
| *RUNX2* | GCCGGGAATGATGAGAACTA | GGACCGTCCACTGTCACTTT |
| *COL1* | CGCTGGCAAGAATGGCGATC | ATGCCTCTGTCACCTTGTTCG |
| *GAPDH* | TGAACTAACACAGAGGAGGATCAG | GCTTAGGGCATGAGCTTGAC |

quality controls (QCs), and samples, were equilibrated to room temperature before use. Working solutions were prepared as instructed by the kit. The required number of ELISA strips was removed from the aluminum foil pouch, while the remaining strips were resealed in a self-sealing bag and stored at 4°C. Wells were designated for standards, 0 value, blanks, and samples. Each standard received 50 μL of standards at different concentrations, 0 value wells received 50 μL of sample diluent, blank wells were left empty, and sample wells received 50 μL of test samples. Then, 100 μL of horseradish peroxidase (HRP)-labeled detection antibody was added to all standard, 0 value, and sample wells. Plates were sealed and incubated at 37°C for 60 min in a water bath or thermostat. After incubation, the sealing film was removed, the liquid was discarded, and the plate was gently blotted dry with absorbent paper. Each well was then filled with washing solution and allowed to stand for 20 s. The reaction plate was then shaken with washing solution, and the plate was patted dry with absorbent paper; this process was repeated five times. If an automatic plate washer was used, the plate was washed according to the manufacturer's instructions, with a 30-s programmed soak included to improve assay precision. After the final wash, the plate was thoroughly blotted dry on clean, non-abrasive paper. Substrate solutions A and B were mixed in a 1:1 volume ratio, and 100 μL of the mixture was added to each well. The plate was then covered with sealing film and incubated in the dark at 37°C for 15 min in a water bath or thermostat. After incubation, 50 μL of stop solution was added to each well, and the absorbance (OD) of each well was measured at 450 nm using a microplate reader.

### 2.5. *In vivo* assessment of osteogenic performance of scaffolds

#### *2.5.1. Establishment of rat cranial defect model*

In order to test the bone reparative ability of the scaffold material *in vivo*, a model of bilateral bone defects in the skull of SD rats was established. The scaffolds were cylindrical (diameter: 5 mm; height: 1 mm) and were irradiated and sterilized (10 kGy) before implantation.

The animal experimental study was approved by the Animal Ethics Committee of Zunyi Medical University (approval no. ZMU21-2412-019). The animal model was established with 36 SD rats (280–320 g), kept under the same conditions. The rats were randomly distributed into the blank, P, SBP, and PSBP groups, respectively. Bone regeneration was assessed using a bilateral critical-sized cranial defect model (5 mm diameter), with the defect area in the cranial bone measuring approximately 5 mm in diameter and 2 mm in height. Scaffolds from the three groups—P, SBP, and PSBP—were implanted into the defect sites, and the scalp was sutured.

The animal model was developed as described herein. SD rats were weighed and anesthetized. The surgical area of the skull was shaved, the animals were fixed in the prone position, disinfected with 1% iodophor, and covered with sterile sheets. A midline incision approximately 2 cm in length was made along the cranial vault, and the subcutaneous tissue was separated using the handle of a scalpel. The periosteum was neatly incised along the sagittal suture of the skull, and the subperiosteal tissues were carefully peeled off with the handle of the scalpel, fully exposing the parietal, occipital, and part of the frontal bone bilaterally. A 5-mm diameter round full-layer bone defect was created on both sides of the parietal midline of the rat skull using a low-speed hollow ring drill (1400–1500 rpm), taking care to avoid damaging the dura mater. At the start of drilling, gentle manual pressure was applied to initiate cranial penetration, which was reduced near completion to prevent injury to the underlying dura and blood vessels. The drill was then tilted at an angle of 20°–30° in forward, backward, left, and right directions without additional external force, allowing gravity to facilitate intermittent

penetration of the cranial bone. A small number of the cranial connections were retained. After testing the skull with ophthalmic forceps for looseness, the skull was removed along the peripheral circular defect. The defect area was repeatedly rinsed with saline, and the scaffold was implanted into the cranial defect site of rats; no material was placed in the blank group. The wound was closed using a 4-0 absorbable suture, and antibiotics were injected for 3 consecutive days postoperation to prevent infection. The implantation process of the scaffold is presented in Figure 2A–C.

#### 2.5.2. Postoperative observational indicators

Vital signs, activity, diet, urination and defecation, and incision recovery of SD rats were observed after surgery, with particular attention paid to the presence of abdominal distension to prevent the occurrence of intestinal obstruction.

#### 2.5.3. Specimen collection

At 1, 2, and 3 months post-surgery, SD rats were euthanized to obtain liver, kidney, and skull specimens, which were immersed in 4% paraformaldehyde.

#### 2.5.4. Hematoxylin and eosin staining

Rat liver, kidney, and skull specimens with completed decalcification were fixed, embedded, and sectioned. Paraffin sections were deparaffinized in water by sequential immersion in xylene for 20 min (twice), followed by 95% ethanol for 5 min, 80% ethanol for 5 min, and 75% ethanol for 5 min, before washing them with tap water.

Frozen sections were removed from a –20°C freezer and brought to room temperature. The sections were fixed with tissue fixative for 15 min and then rinsed with running water. For pretreatment, the sections were treated with "HD Constant Staining Pretreatment Solution" for 1 min. The sections were then stained with hematoxylin staining solution for 3–5 min, washed with tap water, differentiated with differentiation solution, washed again with tap water, returned to blue using the "Return to Blue Solution," and finally rinsed with running water. Later, the slices were dehydrated in 95% alcohol for 1 min, then stained in an eosin staining solution for 15 s. The sections were sequentially dehydrated in 80% anhydrous ethanol (2 min), 95% ethanol (2 min), and 100% ethanol (2 min), followed by clearing in n-butanol (2 × 2 min) and xylene (2 × 2 min). Sections were then mounted using neutral gum. Under a light microscope, the nuclei appeared blue and the cytoplasm red.

#### 2.5.5. Masson staining

Cranial specimens with completed decalcification were fixed, embedded, and sectioned. Paraffin sections were deparaffinized in water by sequential immersion in xylene for 20 min (twice), followed by 95% ethanol for 5 min, 80% ethanol for 5 min, and 75% ethanol for 5 min, before washing with tap water.

Frozen sections were removed from the –20°C freezer, brought to room temperature, fixed with tissue fixative for 15 min, and rinsed with running water. The sections were immersed in Weigert's iron hematoxylin solution overnight, followed by rinsing under running tap water. Sections were immersed in a 1:1 mixture of Lichun Red Acidic Compound Red solution (a mixed dyeing solution composed of the main dyes Acid Red 112 and Acid Red 87) and 1% phosphomolybdic acid aqueous solution for 1 min, washed with tap water, differentiated for a few seconds in differentiation solution, and finally rinsed with tap water. The slices were stained with aniline blue solution for 6 min and then rinsed in tap water. They were subsequently immersed in 0.2% glacial acetic acid for 1 min. Without

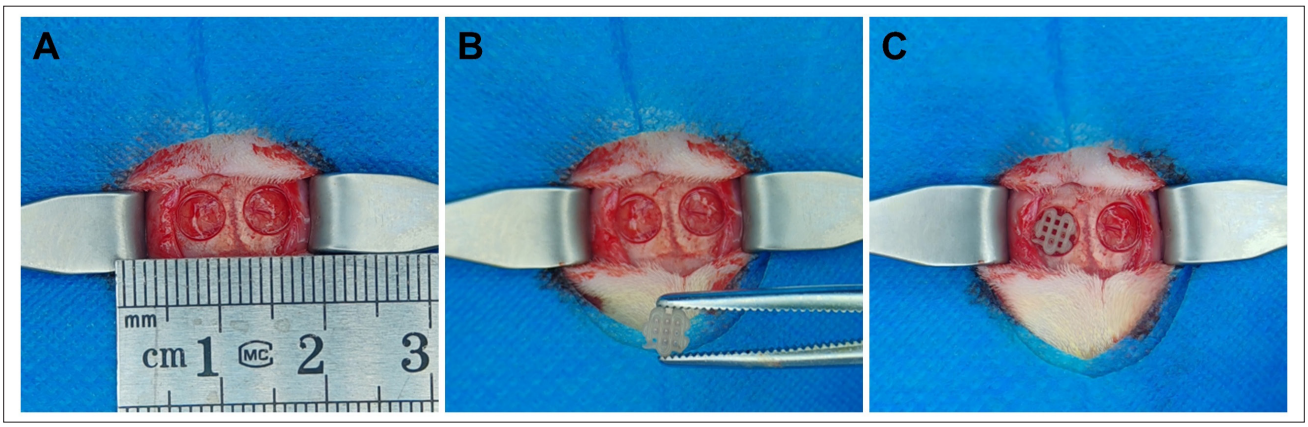


**Figure 2.** Preparation of the bilateral cranial bone defect model (diameter: 5 mm) and implantation of scaffolds in SD rats. (A) Establishment of bilateral cranial defects in SD rats. (B) Scaffolds implantation process. (C) Scaffolds implantation in the defect area. Abbreviation: SD, Sprague-Dawley.

further washing, the slices were drained and directly stained in 1% hydrochloric acid in alcohol for 2–30 s. After rinsing, the sections were further differentiated with 1% acetic acid and dehydrated in two tanks of anhydrous ethanol (75% and 95%). For sealing, the sections were immersed in a third vat of anhydrous ethanol (99%) for 5 min, xylene for 5 min for transparency, and sealed with neutral gum. Collagen fibers appeared blue, while myofibrils, fibrin, and erythrocytes were stained red under a light microscope.

#### *2.5.6. Micro-computed tomography*

Micro-computed tomography (micro-CT) analysis was performed using a ZKKS-MCT-Sharp scanner (Zhong Ke Kai Sheng, China). Cranial specimens from each group at 1-, 2-, and 3-months post-operation were fixed in the scanner along the long axis. Scanning parameters were set as follows: voltage at 70 kV, power at 7 W, four-frame superimposition, an angular gain of 0.72°, and an exposure time of 100 ms. Each sample was rotated 360° to complete the scan. The scanned images were denoised and reconstructed to obtain 3D images. Bone repair and bone growth in the cranial defects of rats were observed; the bone volume fraction of the newborn bone in the cranial defects of rats was calculated using a Bruker high-resolution micro CT (CTAn). Finally, the cranial micro-CT data of rats from different subgroups were statistically analyzed to compare the differences.

#### *2.5.7. Immunofluorescence staining*

The SD rats were euthanized at postoperative months 1, 2, and 3, and the cranial tissues were removed and fixed in 4% paraformaldehyde for 48 h. The cranial specimens were then placed in a 10% EDTA demineralization solution for decalcification. To determine the new bone formation, hematoxylin and eosin (HE) staining, Masson staining, and immunofluorescence staining were performed on the sections of each sample. Sections with 5 μm thickness were cut from paraffin-embedded tissues for histological assessment. These sections were immersed in 3% (w/v) $H_2O_2$ and blocked with 3% (v/v) Bull serum albumin (BSA) solution. After enzymatic antigen repair, the sections were again incubated with the following primary antibodies: BMP-2 (rat, 1:100 dilution; Abcam, USA); VEGF (rat, 1:200 dilution; Abcam, USA); CD163 (rat, 1:100 dilution; Abcam, USA); and iNOS (rat, 1:2000 dilution; Abcam, USA). After rinsing twice with PBS, the samples were incubated with the corresponding horseradish peroxidase-labeled secondary antibodies and then visualized by staining with 4',6-diamidino-2-phenylindole (DAPI). Cell nuclei were stained with hematoxylin.

### 2.6. Statistical analysis

Data were processed using SPSS 29.0 software (IBM, China). The experimental data were expressed as mean ± standard deviation, and comparisons between groups were statistically analyzed using one-way analysis of variance (ANOVA) and independent samples *t*-tests. Graphs were plotted using GraphPad Prism (GraphPad Software, America) and Origin software (Beijing Tianyan Rongzhi Software Co., Ltd, China). Statistically significant differences are indicated by $^{*}p < 0.05$, $^{**}p < 0.01$, and $^{***}p < 0.001$.

## 3. Results

### 3.1. Scaffold preparation and characterization

#### *3.1.1. Characterization of SrBG*

The microscopic morphology of SrBG was characterized using SEM. The SrBG prepared consisted of many regular stacks of small particles with well-dispersed glass particles arranged in clusters (Figure 3A). DLS analysis (Figure 3B) revealed that the SrBG particle size distribution was 350–700 nm, with the most prevalent size being 493.9 nm, accounting for about 38% of the total distribution.

#### *3.1.2. Characterization and physicochemical properties of P, SBP, and PSBP scaffolds*

The surface morphology of the composite scaffolds (P, SBP, and PSBP) is presented in Figure 4A. Compared to the P scaffolds, the pore size of the SBP scaffolds did not change significantly, and the surface became roughened by the addition of SrBG. The surface of the SBP scaffolds had SrBG particles attached, but the pores on the surface became smaller, and the number of pores decreased. After the addition of PDA to the SBP scaffolds, there was no significant change in the pore size of the scaffolds, but the number of pores was further reduced, mainly because the PDA coating covered the original pores. At higher magnification (× 2000), the surface of PSBP scaffolds was smoother compared to the SBP scaffolds, and SrBG particle attachment was observed on the surface of PSBP scaffolds. The porosity of the P, SBP, and PSBP scaffolds was 68.29 ± 5.62%, 65.00 ± 2.62%, and 60.53 ± 2.87%, respectively (Figure 4C). The porosity of the PSBP scaffold was slightly lower than that of the P and SBP scaffolds, but the difference was not significant, consistent with the results of SEM. The contact angles of the scaffolds in each group were examined by the static contact angle method (Figure 4B1); the contact angles of the P, SBP, and PSBP scaffolds were 99.01 ± 2.62°, 72.04 ± 2.27°, and 0°, respectively (Figure 4B2). Generally, a smaller contact angle would indicate a more hydrophilic material. Overall, the addition of PDA and SrBG significantly improved the hydrophilicity of PCL materials, and the PSBP scaffolds had better hydrophilicity compared to the P and SBP scaffolds. The SBP and PSBP scaffolds were immersed in PBS, and the release of $Sr^{2+}$ was measured on days 1 and 3. The SBP and PSBP scaffolds

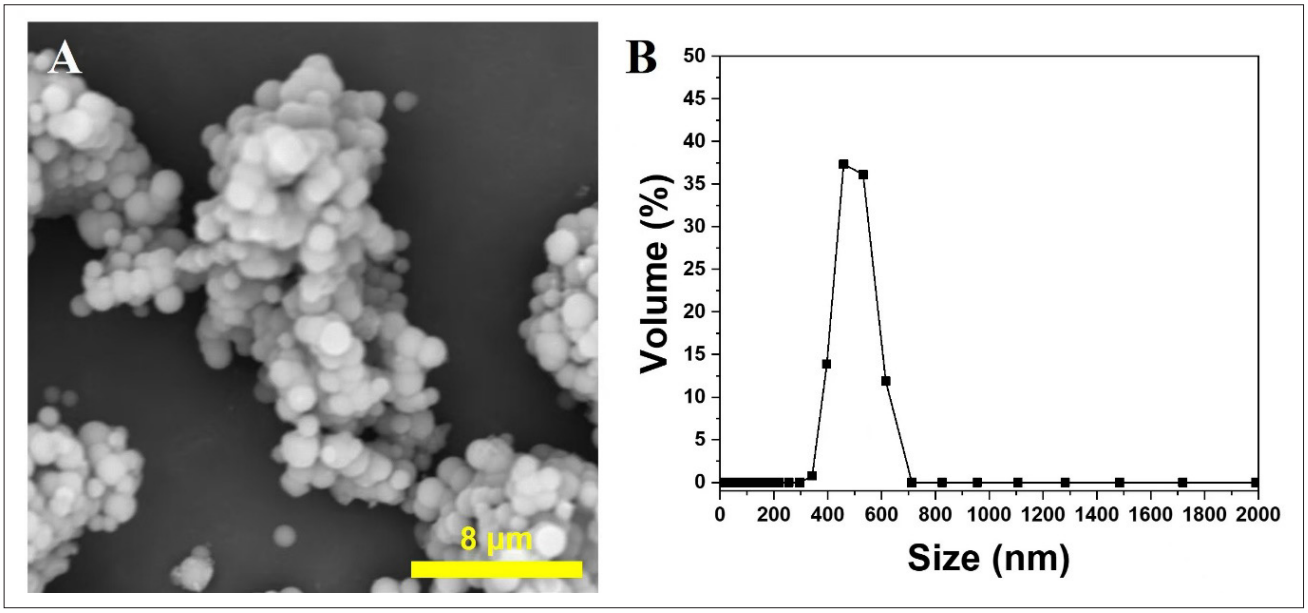


**Figure 3.** Characterization of SrBG. (A) SEM image of the surface morphology of SrBG. (B) Particle size distribution of SrBG. Scale bar: 8 μm (A). Abbreviations: SEM, scanning electron microscope; SrBG, strontium doped bioglass.

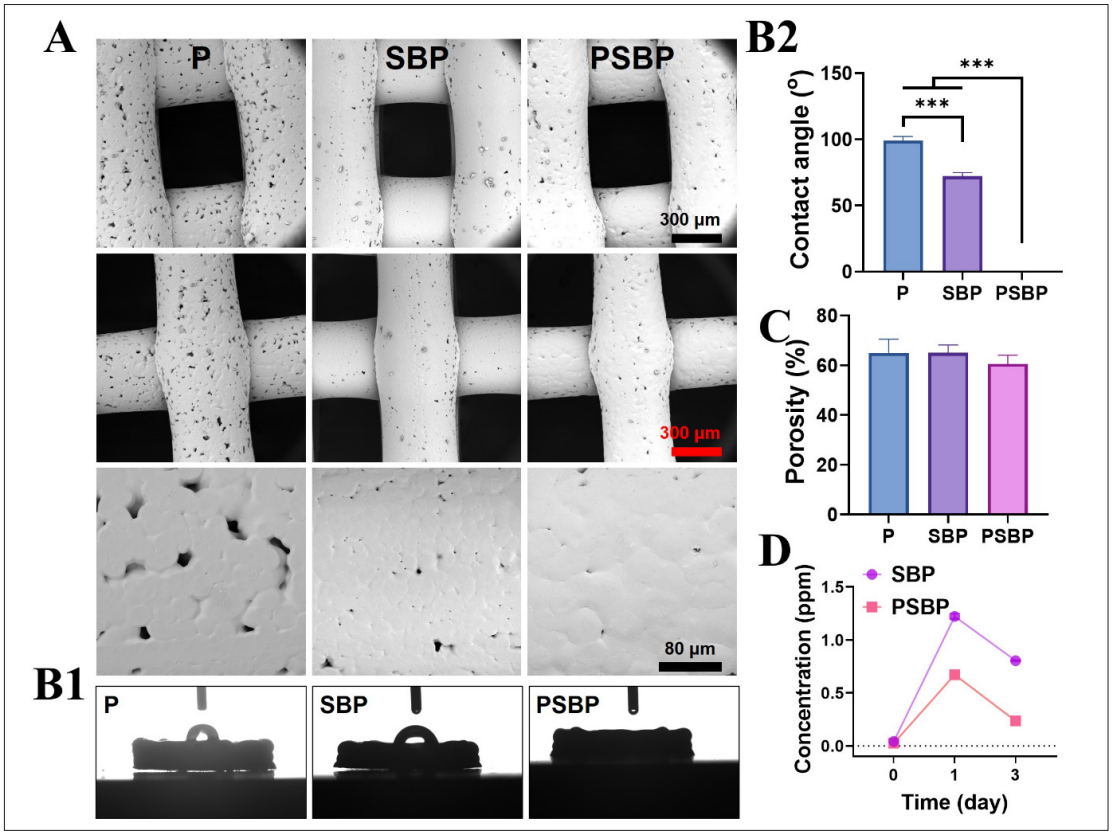


**Figure 4.** Characterization of each group of stents. (A) SEM images of the P, SBP, and PSBP scaffold surface. (B1 and B2) Contact angle and hydrophilicity analysis of P, SBP, and PSBP scaffolds. Static water contact angle photos of the stents (B1) Static water contact Angle data of the stents (B2) ($n = 3$; ***$p < 0.001$). (C) Porosity analysis of P, SBP, and PSBP scaffolds ($n = 6$). (D) $Sr^{2+}$ release from SBP and PSBP scaffolds. Scale bars: 300 μm (A, top and middle); 80 μm (A, bottom). Abbreviations: P, polycaprolactone (PCL); PSBP, polydopamine (PDA)/strontium (Sr)-doped bioactive glass (SrBG)/polycaprolactone (PCL); SBP, strontium (Sr)-doped bioactive glass (SrBG)/polycaprolactone (PCL); SEM, scanning electron microscope.

continuously released $Sr^{2+}$ over time, but the total $Sr^{2+}$ released from the PSBP scaffolds was lower than that of the SBP scaffolds (Figure 4D).

Thermogravimetric analyses of the P, SBP, and PSBP scaffolds were performed accordingly. The thermogravimetric analysis (TG) curves in Figure 5A revealed that all three groups of scaffolds started to decompose at 250–300°C. The P scaffold displayed weight loss at approximately 300°C, and no further weight loss was observed at approximately 450°C; the SBP and PSBP scaffolds exhibited weight loss at approximately 250°C, and no further weight loss was observed at approximately 350°C. These observations suggest that the SBP and PSBP scaffolds had higher thermal stability than the P scaffolds. Thermogravimetric analysis revealed that the weight loss of the P, SBP, and PSBP scaffolds was 97.73%, 89.35%, and 88.78%, respectively. The residual inorganic content in each scaffold closely matched the theoretical proportions of the incorporated SrBG (0%, 9.09%, and 9.09%, respectively). The mechanical properties of the P, SBP, and PSBP scaffolds were examined by compressive testing experiments. The compressive strengths of the P, SBP, and PSBP scaffolds were 5.47 ± 1.41, 15.96 ± 0.87, and 22.52 ± 3.69 MPa, respectively (Figure 5B1). The compressive modulus of the P, SBP, and PSBP scaffolds was 1166.30 ± 314.05, 3321.26 ± 24.21, and 4878.65 ± 398.81 MPa, respectively (Figure 5B2). With the gradual addition of SrBG and PDA, the compressive strength and compressive modulus of the P, SBP, and PSBP scaffolds gradually increased, and the difference was statistically significant ($p < 0.05$).

### 3.2. *In vitro* experimental results

#### *3.2.1. Biocompatibility of P, SBP, and PSBP scaffolds*

To observe the cellular activity of the scaffolds, the composite P, SBP, and PSBP scaffolds were co-cultured with BMSCs for 3 days and subsequently observed by live-dead cell staining. The fluorescence on the PSBP scaffold was more obvious than that in the P and SBP scaffolds, and the amount of adhered BMSCs was significantly higher in the PSBP scaffold compared to the P and SBP scaffolds; only a small amount of BMSCs were attached to the SBP scaffold, while almost no BMSCs were observed on the P scaffold (Figure 6A). These observations suggest that the PSBP scaffold was the most favorable for cell adhesion and proliferation. To assess the potential cytotoxicity and cell proliferation of the P, SBP, and PSBP scaffolds, a CCK-8 cell proliferation assay was performed. The P, SBP, and PSBP scaffolds were co-cultured with BMSCs for 1, 3, and 7 days. After 1 day of co-culture, no significant difference in cell proliferation was observed between the three scaffold groups; after 3 days of co-culture, cell proliferation in the PSBP scaffold was significantly higher

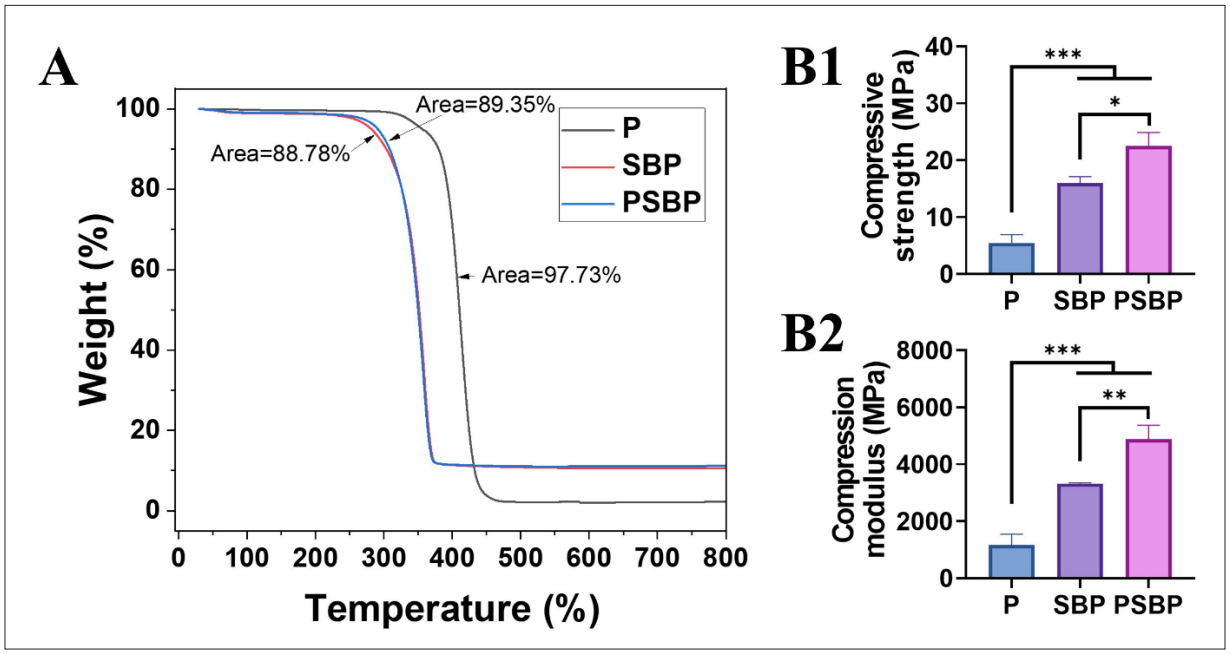


**Figure 5.** Thermodynamic and compressive performance characterization of the support. (A). Thermogravimetric analysis of the P, SBP, and PSBP scaffolds to evaluate their thermal stability and decomposition behavior. (B1 and B2) The compressive strength (B1) and compression modulus (B2) of the P, SBP, and PSBP scaffolds (n = 3; *p < 0.05, **p < 0.01, ***p < 0.001). Abbreviations: P, polycaprolactone (PCL); PSBP, polydopamine (PDA)/strontium (Sr)-doped bioactive glass (SrBG)/polycaprolactone (PCL); SBP, strontium (Sr)-doped bioactive glass (SrBG)/polycaprolactone (PCL).

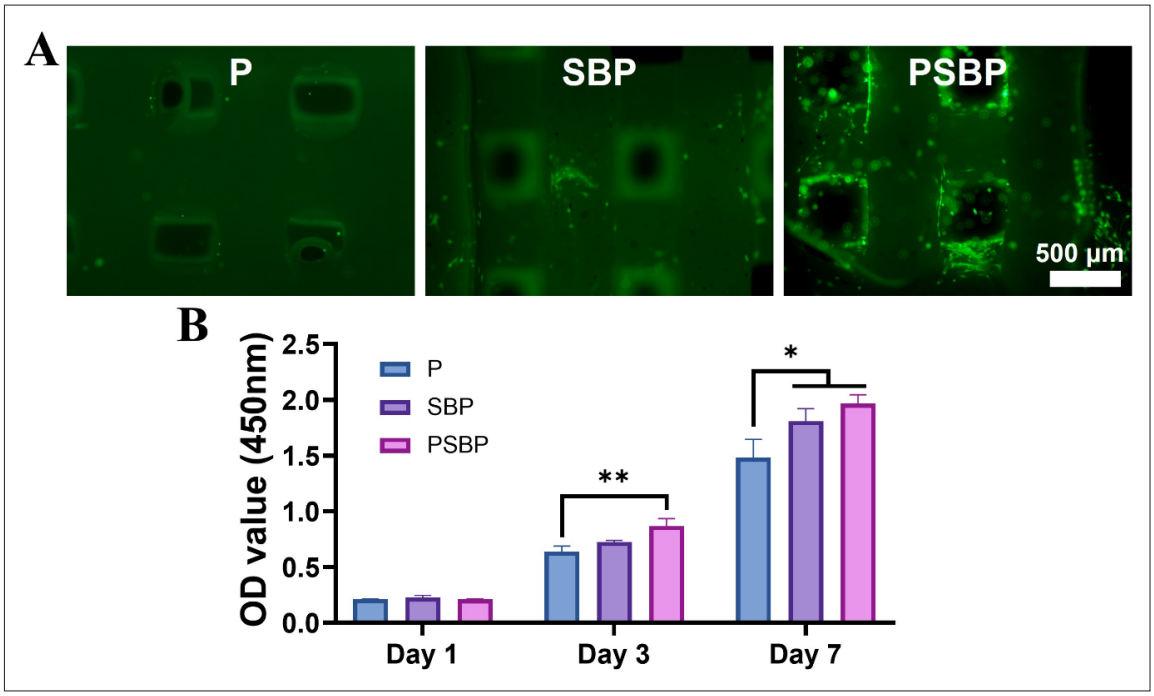


**Figure 6.** BMSCs viability assay on scaffolds. (A) Live-dead cell staining after 3 days of co-culturing BMSCs within P, SBP, and PSBP scaffolds. (B) Cell proliferation within the P, SBP, and PSBP scaffolds on days 1, 3, and 7 ($n = 3$; $^{*}p < 0.05$, $^{**}p < 0.01$). Scale bar: 500 μm (A). Abbreviations: BMSCs, bone marrow mesenchymal stem cells; OD, optical density; P, polycaprolactone (PCL); PSBP, Polydopamine (PDA)/strontium (Sr)-doped bioactive glass (SrBG)/polycaprolactone (PCL); SBP, strontium (Sr)-doped bioactive glass (SrBG)/polycaprolactone (PCL).

than that in the P scaffold ($p < 0.01$); after 7 days of co-culture, cell proliferation in the PSBP and SBP scaffolds was significantly higher compared to the P scaffold ($p < 0.05$).

#### *3.2.2. Bone-enhancing properties of P, SBP, and PSBP scaffolds*

To assess the early osteogenic activity of the scaffolds, the P, SBP, and PSBP scaffolds were co-cultured with BMSCs for 7 days and then subjected to ALP staining. The P scaffold exhibited weaker and lighter ALP staining, indicating a limited effect on promoting osteoblast differentiation. In contrast, the SBP scaffold, which included SrBG, displayed markedly increased and intensified intracellular ALP staining. The PSBP scaffold, incorporating both SrBG and PDA, demonstrated the most pronounced ALP staining, suggesting a synergistic enhancement of osteogenic differentiation (Figure 7A1). The ALP activity in the PSBP scaffold was significantly higher than that in the P and SBP scaffolds ($p \leq 0.001$) (Figure 7A2). To assess the effects of the scaffolds on the osteogenic differentiation of BMSCs, the expression of osteogenesis-related genes (*COL1*, *ALP*, and *RUNX2*) was assessed after co-culturing BMSCs with the scaffolds for 7 and 14 days in MP medium. The expressions of *COL1*, *ALP*, and *RUNX2* were significantly upregulated in the PSBP scaffold compared to the P and SBP scaffolds, suggesting a positive effect on bone differentiation. On day 14, *ALP* expression in the PSBP scaffold was 7.1 and 2.4 times higher than that in the SBP and P scaffolds, respectively; *RUNX2* expression in the PSBP scaffold was 10.3 and 3.2 times higher than that in the SBP and P scaffolds, respectively; and *COL1* expression in the PSBP scaffold was 8.5 and 7.1 times higher than that in the SBP and P scaffolds, respectively (Figure 7B). These observations indicate that the PSBP scaffold had better immunomodulatory ability to promote the osteogenic differentiation of BMSCs compared to the P and SBP scaffolds ($p < 0.05$).

#### *3.2.3. Immunomodulatory capacity of P, SBP, and PSBP scaffolds*

To assess the immunomodulatory properties of the scaffolds, the expression of MP polarization-related genes was detected by co-culturing RAW264.7 cells with the P, SBP, and PSBP scaffolds for 1 and 3 days. The expression of M2-MP polarization genes (*CD206* and *ARG*) was significantly upregulated in the PSBP scaffold compared to the P and SBP scaffolds (Figure 8A3 and A4). In contrast, the PSBP scaffold significantly inhibited the expression of M1–MP polarization genes (*TNF-α* and *IL1β*) (Figure 8A1 and A2). On day 3, *ARG* gene expression in the PSBP scaffold was 7.1 and 4.3 times higher than that in the

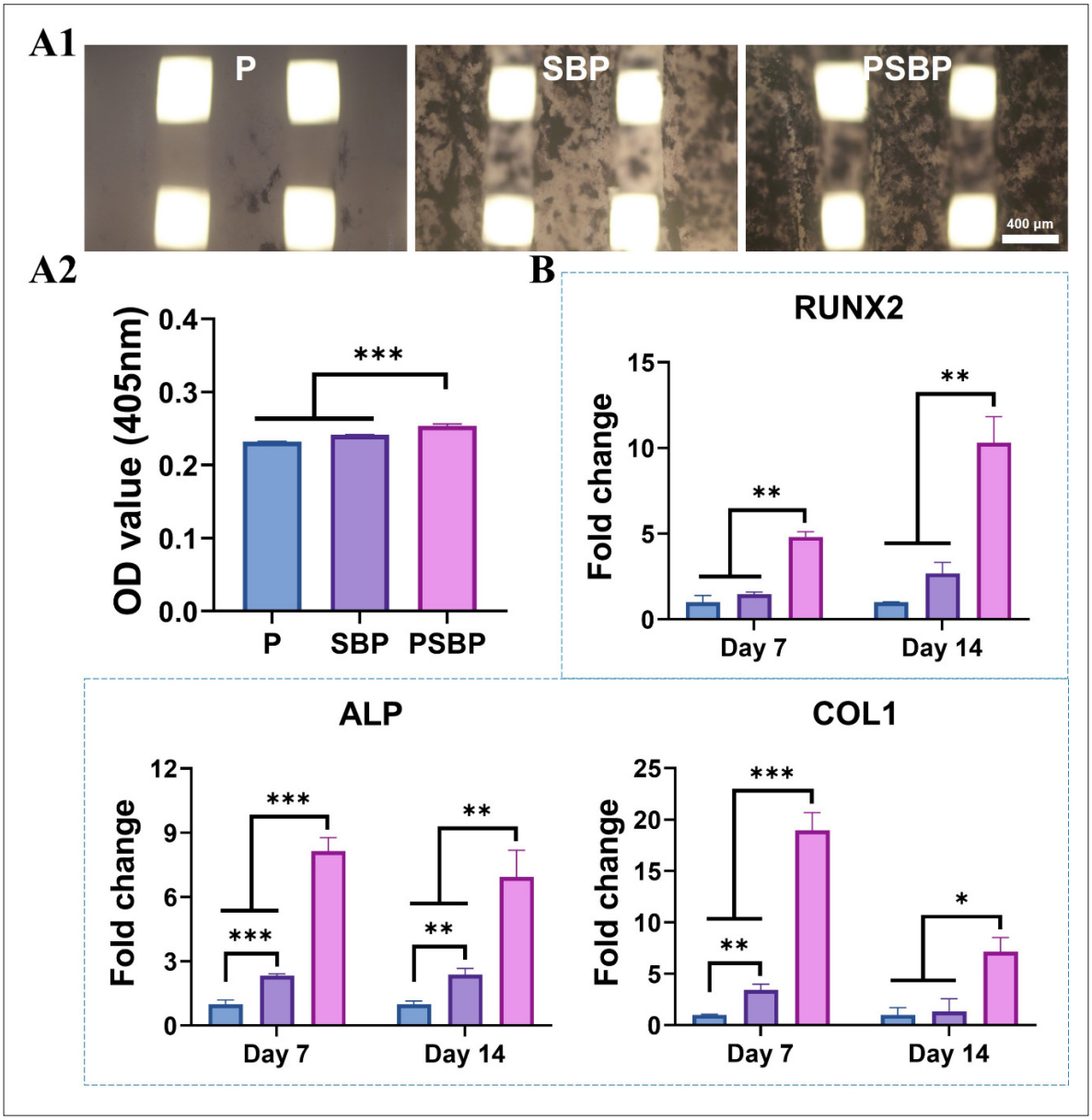


**Figure 7**. The effect of scaffolds on the osteogenic differentiation performance of BMSCs in vitro. (A1 and A2) ALP staining (A1) and ALP activity analysis (A2) of P, SBP, and PSBP scaffolds co-cultured with BMSCs. (B) Expression of osteogenesis-related genes in the P, SBP, and PSBP scaffolds co-cultured with BMSCs ($n = 3$; *$p < 0.05$, **$p < 0.01$, ***$p < 0.001$). Scale bar: 400 μm (A1). Abbreviations: BMSCs, bone marrow mesenchymal stem cells; OD, optical density; P, polycaprolactone (PCL); PSBP, polydopamine (PDA)/strontium (Sr)-doped bioactive glass (SrBG)/polycaprolactone (PCL); SBP, strontium (Sr)-doped bioactive glass (SrBG)/polycaprolactone (PCL).

SBP and P scaffolds, respectively; *CD206* gene expression in the PSBP scaffold was 6.5 and 1.6 times higher than that in the SBP and P scaffolds, respectively; *TNF-α* gene expression in the P and SBP scaffolds was 2.3 and 2.6 times higher than that in the PSBP scaffold, respectively; and *IL1β* gene expression in the P and SBP scaffolds was 12.3 and 14.2 times higher than that in the PSBP scaffold, respectively. To further verify the immunomodulatory effect of the scaffolds, the levels of pro-inflammatory factor IL-12 and anti-inflammatory factor IL-10 were detected by ELISA assay. Compared to the SBP scaffold, the PSBP scaffold suppressed the expression level of pro-inflammatory factor IL-12 and increased the expression level of anti-inflammatory factor IL-10 ($p < 0.05$) (Figure 8B1 and B2).

### 3.3. *In vivo* experimental results

#### *3.3.1. Hepatotoxicity and nephrotoxicity of P, SBP, and PSBP scaffolds*

To assess the biosafety of the scaffolds, liver and kidney tissues of rats in each scaffold group were sampled at postoperative months 1, 2, and 3, and tissue sections were HE-stained to observe the presence or absence of lesions in these organs. It was observed that specific structures in the rat liver (Figure 9) and kidney (Figure 10)—such as the central vein, the confluent area, hepatocytes, glomeruli, and mesangial cells—in each scaffold group had a clear morphology and boundaries, with no signs of inflammatory cell infiltration. This suggests that the composite scaffolds have good biocompatibility, as they did not have any toxicity effects on the rat liver and kidney.

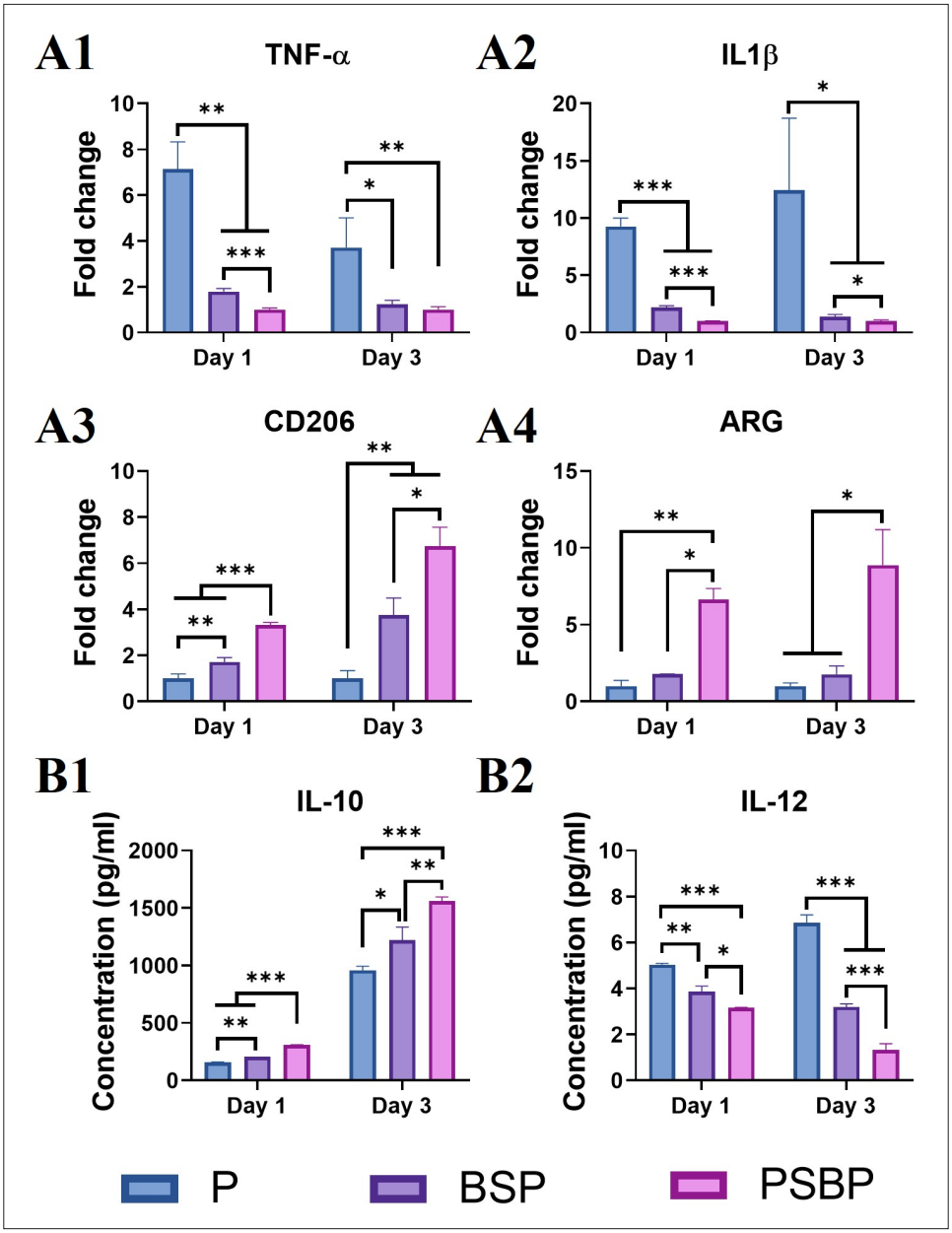


**Figure 8.** The effect of scaffolds on Macrophage Typing Polarization in vitro. (A1–A4) Expression of macrophage polarization-related genes on P, SBP, and PSBP scaffolds: *TNF-α* (A1), *IL1β* (A2), *CD206* (A3), and *ARG* (A4). (B1 and B2) Expression levels of IL-10 (B2) and IL-12 (B1) in the P, SBP, and PSBP scaffolds. $n = 3$; $^{*}p < 0.05$, $^{**}p < 0.01$, $^{***}p < 0.001$. Abbreviations: P, polycaprolactone (PCL); PSBP, polydopamine (PDA)/strontium (Sr)-doped bioactive glass (SrBG)/polycaprolactone (PCL); SBP, strontium (Sr)-doped bioactive glass (SrBG)/polycaprolactone (PCL).

#### *3.3.2. Micro-CT of rat skull*

In order to evaluate the bone repair effect of the three scaffolds *in vivo*, we constructed a bone defect model in SD rats and performed cranial bone sampling at postoperative months 1, 2, and 3; micro-CT scanning was performed to evaluate the repair of the bone defect area. As displayed in Figure 11A, in the blank group, the amount of new bone production in the bone defect area was low at postoperative months 1 and 2, and there was still no significant increase in new bone tissue at postoperative month 3, indicating that the bone repair effect was relatively poor in the absence of scaffolding implantation. Conversely, in the P scaffold, there was a low amount of new bone production at postoperative month 1, and in months 2 and 3, increasing new bone tissue was observed, but large bone defects remained visible, indicating that the bone repair ability of the P scaffold was limited. Compared to the P scaffold, the SBP scaffold—with the addition of SrBG—displayed bone growth along the composite scaffold in the defective area at month 1, gradually increasing over subsequent months until the bone trabeculae covered almost 50% of the defective area at the end of month 3, indicating that the addition of SrBG could promote the repair of bone defects. In contrast, the PSBP scaffold—with the addition of PDA—displayed more bone growth across all time points compared to the P and SBP scaffolds; the defect area was seen to be significantly filled with bone trabeculae at month 1, gradually increasing in subsequent months until almost complete coverage of the bone defect area with bone trabeculae at the end of month 3. The bone volume fraction (Figure 11B) and bone density (Figure 11C) of the bone defect area in each scaffold group

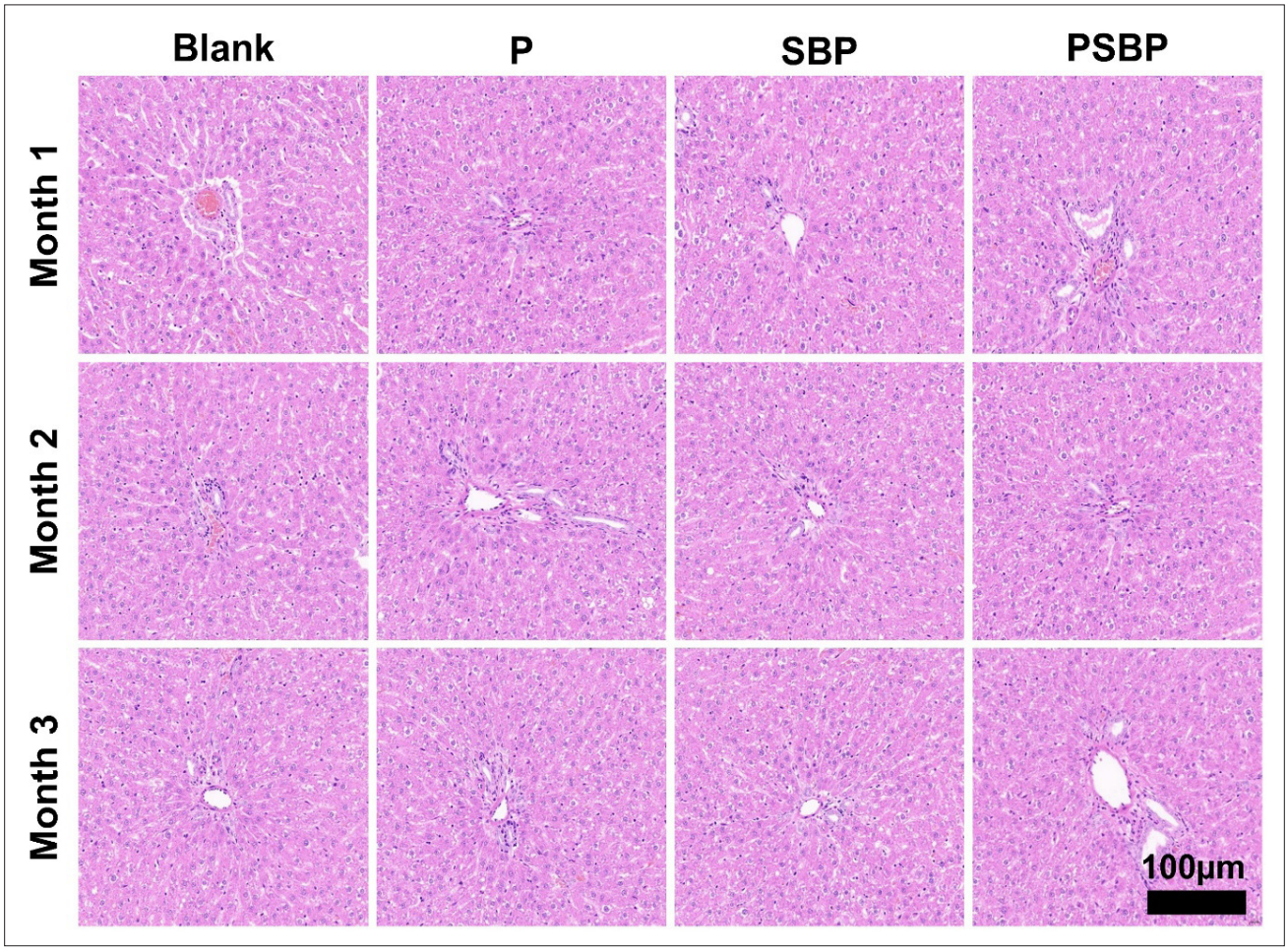


**Figure 9.** Hematoxylin and eosin (HE) staining of rat liver in each scaffold group. Scale bar: 100 μm. Abbreviations: P, polycaprolactone (PCL); PSBP, polydopamine (PDA)/strontium (Sr)-doped bioactive glass (SrBG)/polycaprolactone (PCL); SBP, strontium (Sr)-doped bioactive glass (SrBG)/polycaprolactone (PCL).

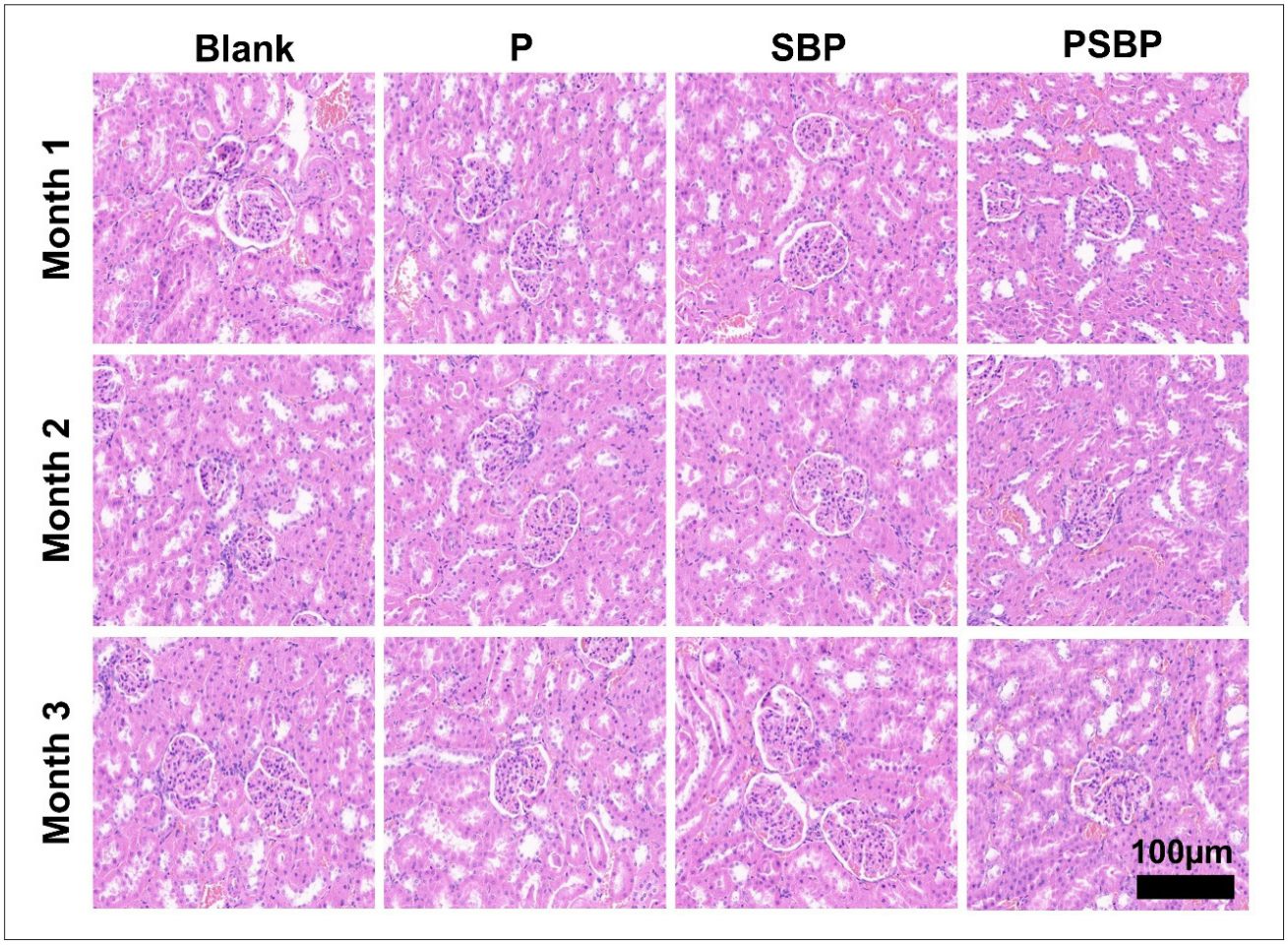


**Figure 10.** Hematoxylin and eosin (HE) staining of rat kidneys in each scaffold group. Scale bar: 100 μm. Abbreviations: P, polycaprolactone (PCL); PSBP, polydopamine (PDA)/strontium (Sr)-doped bioactive glass (SrBG)/polycaprolactone (PCL); SBP, strontium (Sr)-doped bioactive glass (SrBG)/polycaprolactone (PCL).

were statistically analyzed at postoperative months 1, 2, and 3. The PSBP scaffold displayed the best bone repair effect (among the scaffold types) relative to the blank group ($p < 0.05$). The bone mineral density results were consistent with the bone volume fraction analysis.

#### *3.3.3. HE and Masson staining of rat skull specimens*

At 1, 2, and 3 months after surgery, the rats were euthanized; skull specimens were collected and analyzed by HE staining and Masson staining to assess the formation of new bone tissue in the bone defect area. HE staining at postoperative month 1 revealed that the blank group had more fibrous tissue but less new bone tissue in the bone defect area. The P and SBP scaffolds displayed a small amount of new bone in the defect area, while the PSBP scaffold displayed a large amount of new bone formation. At postoperative month 2, the new bone tissue in the PSBP group was progressively darker in color and more widely distributed compared to the other scaffold groups; new bone tissue gradually formed in the pores of the stent, and new bone tissue was observed at the defect interface and inside the material. At postoperative month 3, the new bone tissue in the PSBP group was continuous and more widely distributed, and the area of the new bone was significantly larger than that of the blank, P, and SBP scaffold groups (Figure 12).

The results of Masson staining are displayed in Figure 13. At postoperative month 1, the SBP and PSBP scaffold groups had more light blue collagen tissue and red muscle fiber tissue compared to the blank and P scaffold groups. In subsequent months, the neoplastic bone tissue of each scaffold group further matured, exhibiting dark blue mature collagen, which was most significant in the PSBP scaffold group. These results indicated that PSBP scaffolds could promote bone defect repair.

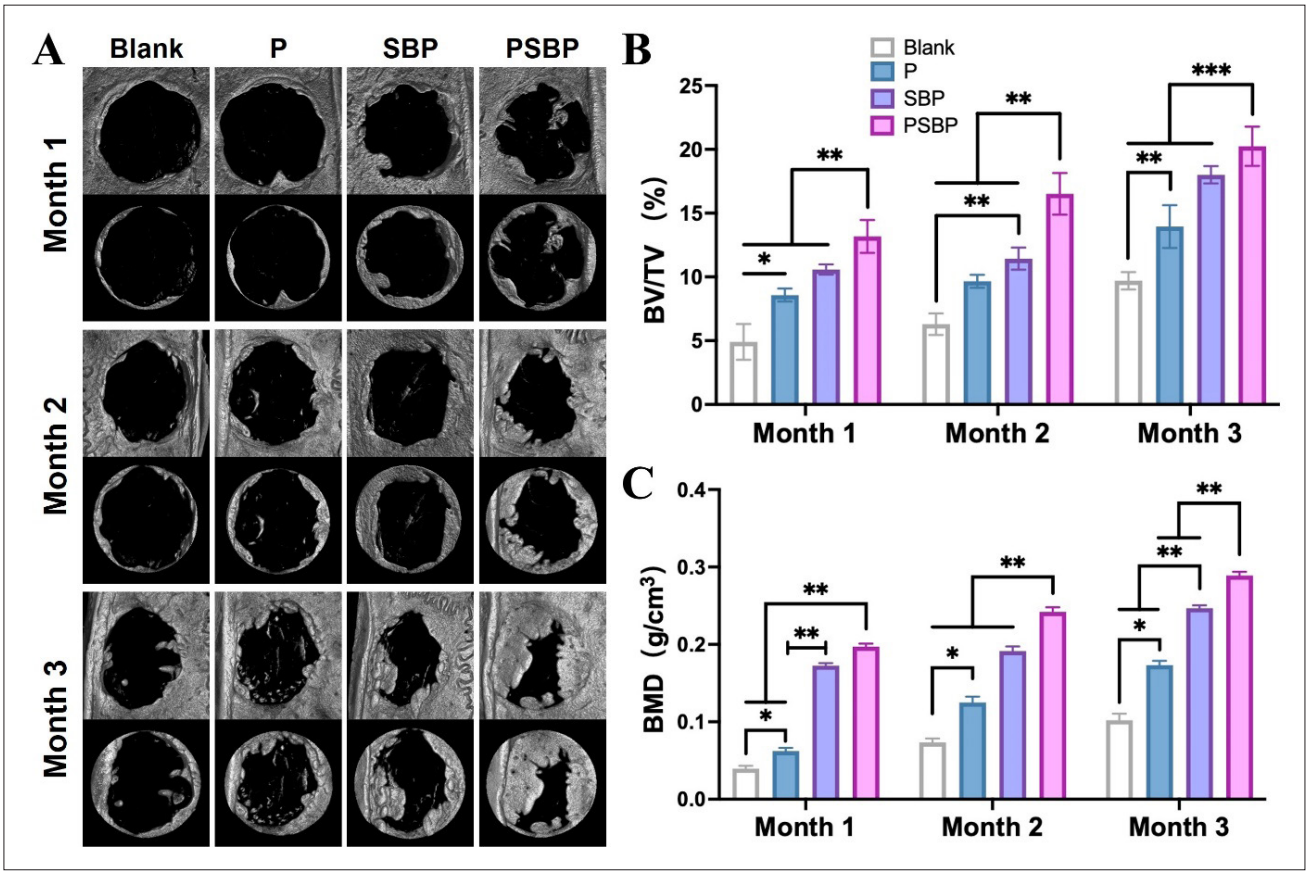


**Figure 11.** Micro-CT assessment of bone defect repair outcomes. (A) Micro-CT analysis of the cranial bone defect area for each scaffold group. (B and C) Bone volume fraction (BV/TV%) (B) and bone mineral density (BMD) (C) in the bone defect area for each scaffold group ($n = 3$; $^{*}p < 0.05$, $^{**}p < 0.01$, $^{***}p < 0.001$). Abbreviations: Micro-CT, micro computed tomography; P, polycaprolactone (PCL); PSBP, polydopamine (PDA)/strontium (Sr)-doped bioactive glass (SrBG)/polycaprolactone (PCL); SBP, strontium (Sr)-doped bioactive glass (SrBG)/polycaprolactone (PCL).

#### *3.3.4. Immunofluorescence staining of rat skull specimens*

To further assess the immunomodulation, pro-angiogenic, and osteogenic differentiation ability of the scaffolds, iNOS (red), CD163 (green), VEGF (red), and BMP-2 (green) were detected by immunofluorescence staining in each scaffold group. The results for immunofluorescence staining are displayed in Figure 14.

In immunomodulation, iNOS and CD163 serve as key markers for MP polarization, representing the M1 and M2 phenotypes, respectively. At postoperative months 1 and 2, the expression of iNOS (red) in new bone tissue in the bone defect area was the highest in the blank group. In contrast, the red fluorescence intensity in the bone defect area progressively decreased across the P, SBP, and PSBP scaffold groups. At postoperative month 3, the PSBP scaffold group had the weakest red fluorescence. Conversely, the expression of CD163 (green) gradually increased over postoperative months 1, 2, and 3, with the PSBP scaffold group emitting the strongest fluorescence at postoperative month 3. These observations suggest that the PSBP scaffolds promoted the expression of M2 MPs and inhibited the expression of M1 MPs, thereby inducing better immunomodulation to facilitate bone defect repair.

In terms of vascularization, at postoperative months 1, 2, and 3, the expression of VEGF (red) in the bone defect area of all groups gradually increased. Among them, the PSBP scaffold group exhibited the strongest fluorescence intensity and the largest expression area, indicating that PSBP scaffolds more effectively promoted vascularization in the bone defect area, thereby facilitating bone defect repair.

In terms of osteogenesis, at postoperative months 1, 2, and 3, the expression of BMP-2 (green) was the lowest in the blank group, but gradually increased in the P, SBP, and PSBP scaffold groups. At postoperative month 3, the PSBP

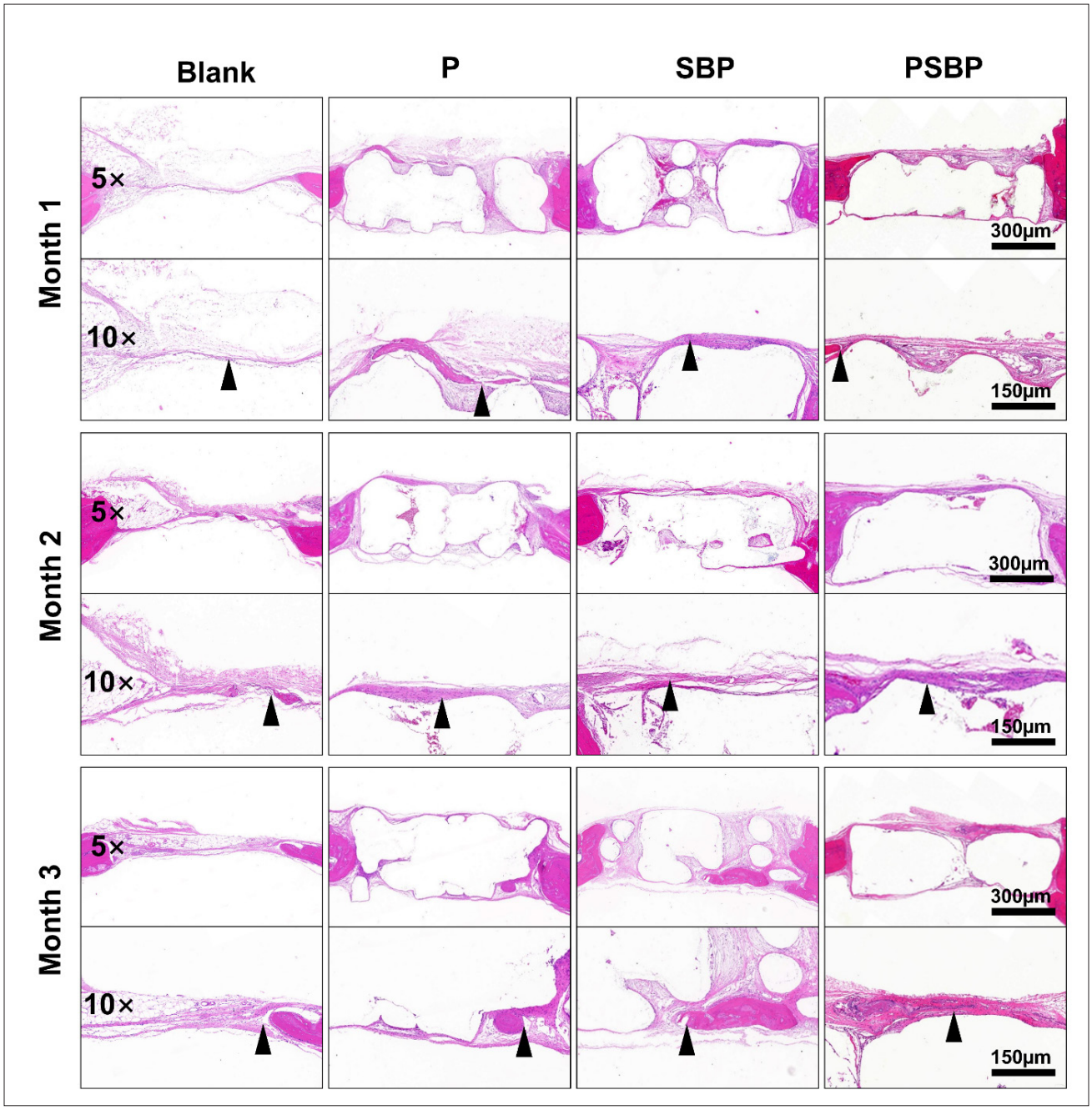


**Figure 12.** Hematoxylin and eosin (HE) staining of the bone defect area of rats in each scaffold group. Arrows indicate area of new bone. Scale bars: 300 μm (top, 5×), 150 μm (bottom, 10×). Abbreviations: P, polycaprolactone (PCL); PSBP, polydopamine (PDA)/strontium (Sr)-doped bioactive glass (SrBG)/polycaprolactone (PCL); SBP, strontium (Sr)-doped bioactive glass (SrBG)/polycaprolactone (PCL).

scaffold group exhibited the strongest green fluorescence, with a significantly larger positive staining area compared to the other groups, indicating a superior bone repair effect.

## 4. Discussion

Ideal tissue engineering scaffolds should have good osteoconductivity, biodegradability, plasticity, and a certain degree of mechanical strength to provide a suitable environment for tissue regeneration and cell growth, adhesion, and proliferation.[43] PCL is used as the main material for bone tissue engineering scaffolds due to its high plasticity and biodegradation *in vivo*, providing space for new bone tissue and blood vessels to grow.[44] However, PCL is biologically inert and needs to be compounded

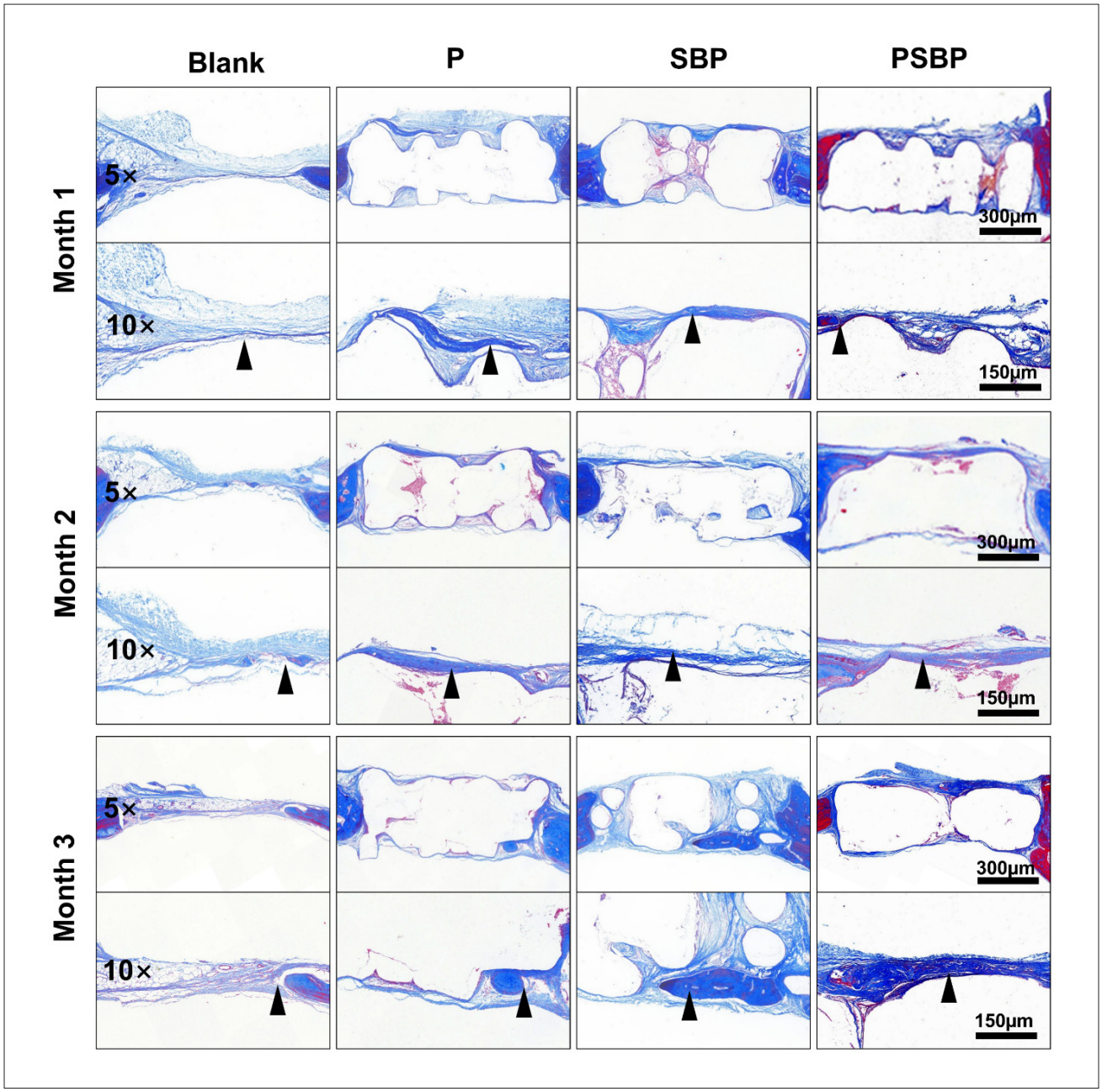


**Figure 13.** Masson staining of the bone defect area of rats in each scaffold group. Arrows indicate area of new bone. Scale bars: 300 μm (top, 5×), 150 μm (bottom, 10×). Abbreviations: P, polycaprolactone (PCL); PSBP, polydopamine (PDA)/strontium (Sr)-doped bioactive glass (SrBG)/polycaprolactone (PCL); SBP, strontium (Sr)-doped bioactive glass (SrBG)/polycaprolactone (PCL).

with other materials for better bone restoration.[45] SrBG has demonstrated certain advantages as a bone repair material due to its good osteogenic ability and immunomodulatory properties.[46] As displayed in Figure 3, SrBG comprises numerous uniformly arranged small spherical particles with a particle size distribution between 350 and 700 nm. Among them, SrBG particles measuring 493.9 nm account for the largest proportion (approximately 38%) of the total, which favors cell adhesion. In addition, functionalization of the material surface with PDA increases the hydrophilicity and surface adhesion of the material, thus effectively improving its biocompatibility.[39,47] Likewise, 3D printing technology can personalize the geometric shape of the scaffold according to the shape of the bone defect, allowing

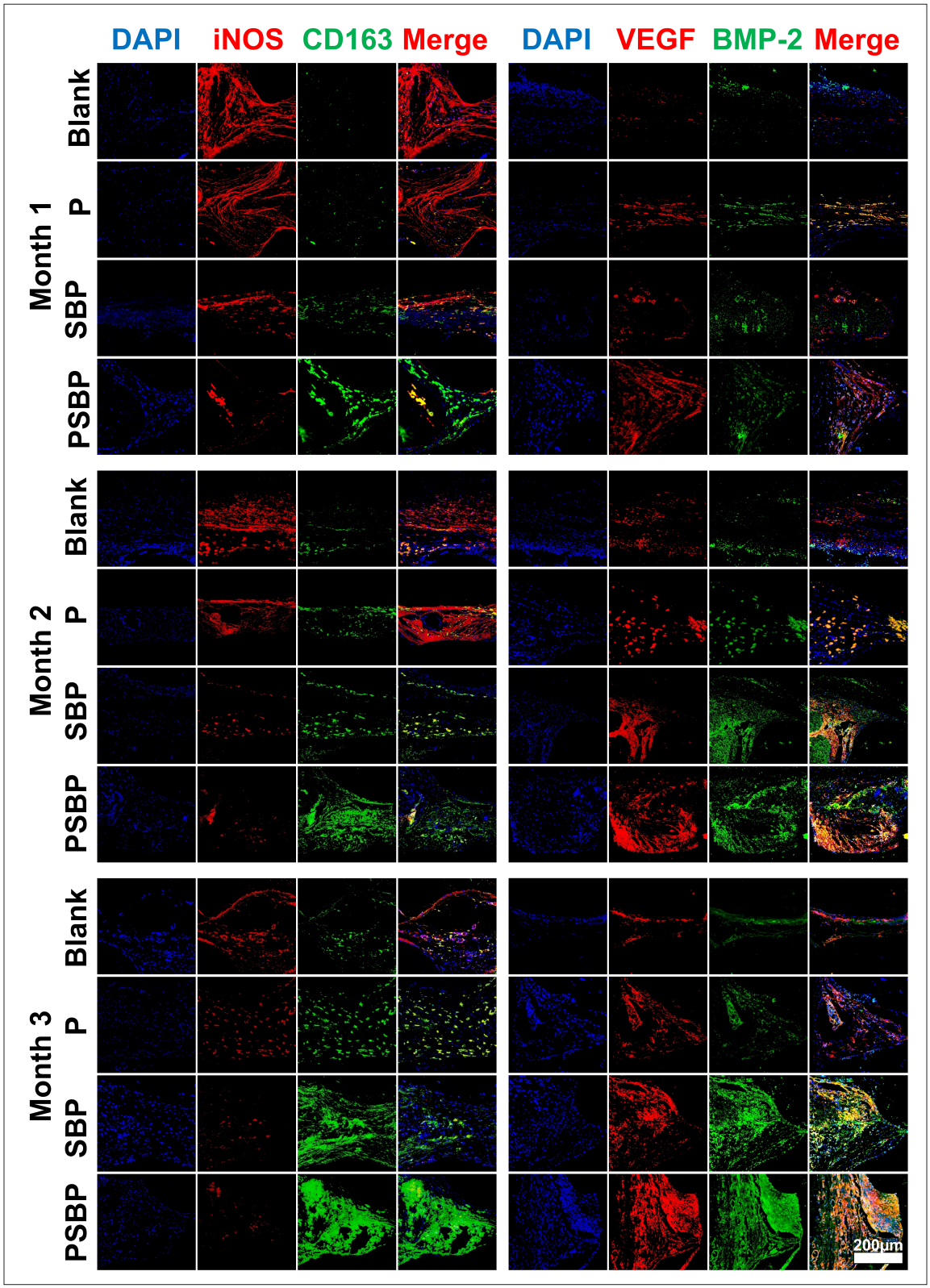


**Figure 14.** Immunofluorescence staining of iNOS, CD163, VEGF, and BMP-2 in the bone defect area of rats in each scaffold group. Scale bar: 200 μm. Abbreviations: P, polycaprolactone (PCL); PSBP, polydopamine (PDA)/strontium (Sr)-doped bioactive glass (SrBG)/polycaprolactone (PCL); SBP, strontium (Sr)-doped bioactive glass (SrBG)/polycaprolactone (PCL).

for better fit at the bone defect site and more effective bone defect repair.[48–50] In this study, P and SBP scaffolds were prepared by 3D printing, and PSBP scaffolds were obtained by co-deposition of PDA with SBP scaffolds. The physical properties, biocompatibility, and immunomodulatory ability of the scaffolds were evaluated by *in vitro* and *in vivo* experiments, and the effects of the scaffolds toward osteogenic differentiation *in vitro* and bone defect repair *in vivo* were assessed.

The three scaffold groups (P, SBP, and PSBP) were characterized accordingly. Firstly, the surface morphology of the scaffolds was observed by SEM (Figure 4A). There was no significant difference in the pore size among the three scaffold groups. However, after SrBG addition and PDA modification, the PSBP scaffolds had SrBG particles attached to their surface, resulting in smaller and fewer surface pores and a smoother surface. Secondly, good porosity is necessary for the scaffold to fulfill its bone repair function.[51] As displayed in Figure 4C, all three scaffold groups exhibited high porosity, with PSBP scaffolds having a slightly lower porosity than P and SBP scaffolds. This is due to the filling of some pores during PDA modification of the SBP scaffolds.[52] It is further demonstrated by the average aperture of each group of scaffolds as shown in Appendix Figure A1, where the smallest average aperture of the scaffolds was observed in the PSBP group. The high porosity of the scaffolds facilitates cell adhesion, growth, and vascular ingrowth.[50] Nonetheless, the differences between the scaffold groups were not significant, and the slight decrease in porosity had little effect on cell growth and angiogenesis. PDA in the PSBP scaffolds filled the fiber pores, significantly enhancing their compressive properties (Figure 5B1 and B2) and inhibiting $Sr^{2+}$ release (Figure 4D) compared to SBP scaffolds. Moreover, filling the porous structure on the fibers increased the scaffolds' compressive strength and reduced their degradation rate, consistent with the trends observed in a previous study.[53] Studies have demonstrated that PDA functionalization of scaffold surfaces strongly attaches reactive groups—such as catecholamines and amines—to the material surface via covalent bonds, thereby improving hydrophilicity, adhesion, and biocompatibility.[54–56] As displayed in Figure 4B1 and B2**,** the PSBP scaffolds featured better hydrophilicity after the addition of SrBG and PDA, providing more favorable conditions for cell adhesion and proliferation. Zhao et al.[57] reported that SrBG effectively improved the mechanical properties and bone repair capability of calcium aluminate cement. In terms of mechanical properties, the compressive strength and modulus of the PSBP scaffolds were significantly higher than those of the P and SBP scaffolds, likely associated with the addition of SrBG and PDA. This suggests that the PSBP scaffolds possessed strong mechanical properties and could withstand greater mechanical loads. In Figure 5A, the thermogravimetric analysis revealed that the mass of the remaining inorganic particles in each scaffold group was close to the theoretical proportion of the mixed SrBG, and all three scaffolds exhibited good thermal stability.

Biocompatibility of the stent is a prerequisite for its biological functioning.[58] As presented in Figure 6A, the results of the live-dead cell assay indicated that the PSBP scaffold had a higher number of adhered and proliferated BMSCs compared to the other scaffold groups, indicating non-cytotoxicity. Meanwhile, results of the CCK-8 proliferation assay indicated that the PSBP scaffold could promote BMSC proliferation significantly better than the other scaffold groups, which was consistent with the live-dead cell staining results. However, the scaffold degradation products post-implantation and the substances generated by their interaction with the body's microenvironment may be potentially toxic to the host.[59] To evaluate the *in vivo* toxicity of the scaffolds, an SD rat model was established in this study. HE staining analysis of liver and kidney tissues revealed no obvious damage or abnormal reaction, highlighting the good biosafety for all three scaffold groups (Figures 9 and 10).

Ideal bone repair materials must be biocompatible and possess strong osteogenic differentiation capacity.[57] However, PCL is limited by its insufficient osteogenic capacity, high hydrophobicity, and lack of sufficient cell attachment sites.[60,61] To overcome these shortcomings, Hench et al.[62] used the sol–gel method to prepare $SiO_2$-CaO-$P_2O_5$ ternary BGs, characterized by numerous microporous structures, a large specific surface area, and a fast rate of surface hydroxyapatite (HA) generation, enabling them to form strong chemical bonds with human bone tissue. In this study, SrBG was compounded in PCL scaffolds, and the scaffolds were modified using PDA to detect osteogenesis-related genes. ALP is a phenotypic marker of early osteogenesis.[63] As displayed in Figure 7A1 and A2**,** the PSBP scaffolds strongly induced osteogenic differentiation, as indicated by ALP activity and staining results. In addition, qRT-PCR revealed that after co-culturing BMSCs with the three scaffold groups under osteogenic induction conditions, the expression of osteogenesis-related genes (*COL1*, *ALP*, and *RUNX2*) was significantly upregulated in the PSBP scaffold group compared to the P and SBP scaffold groups (Figure 7B). This observation was consistent with the ALP activity and staining results.

The immune microenvironment plays a crucial role in bone repair, and MP phenotypic switching is critical for bone defect repair.[64] To regulate the microenvironment's

effect on bone repair, some studies have combined MBG with PCL to prepare MBG/PCL scaffolds that possess better immune-regulating and bone-repair capabilities.[65] Another study prepared SrBG by doping $Sr^{2+}$ into MBG, leading to a significantly enhanced immunomodulatory capacity by promoting M2 MP polarization.[66] The PSBP scaffolds effectively upregulated the expression of M2 MP polarization genes (*CD206* and *ARG*) while suppressing the expression of M1 MP polarization genes (*TNF-α* and *IL1β*) (Figure 8). This may be related to the release of various ions from SrBG, including $Sr^{2+}$, $Si^{4+}$, $Ca^{2+}$, and $P^{5+}$.[67] These ions enhanced the scaffold's immunomodulatory properties by inhibiting M1 MP polarization and promoting M2 MP polarization.[68,69] Results from the $Sr^{2+}$ release experiments demonstrated that $Sr^{2+}$ from the SBP and PSBP scaffolds was continuously released over time (Figure 4D). The overall $Sr^{2+}$ release concentration in the PSBP scaffold group was lower than that in the SBP scaffold group. ELISA experiments indicated that PSBP scaffolds inhibited the expression of the pro-inflammatory factor IL-12 and increased the expression of the anti-inflammatory factor IL-10 at a greater extent compared to SBP scaffolds (Figure 8B1 and B2), suggesting that the relatively low $Sr^{2+}$ concentration in the PSBP scaffolds facilitates better immune microenvironment coordination to promote osteogenesis. Römer et al.[70] found that adding 3 mM (approximately 263 ppm) of $Sr^{2+}$ to the culture medium significantly inhibited the expression of the pro-inflammatory factor IL-6 in human periodontal cells compared to a control group. Buache et al.[71] reported that 10 μM Sr-doped bidirectional calcium phosphate significantly inhibited the expression of TNF-α and IL-6 in human primary monocytes. Both SrBG extracts ($Sr^{2+}$ concentration: 6.227 ppm and 10 μM [approximately 0.88 ppm]), which are obtained after immersing SrBG in cell culture medium and processed, significantly inhibited the expression of TNF-α, IL1β, and IL-6 and elevated the expression of anti-inflammatory factors IL-1ra, IL-10, and Arg-1. Lower $Sr^{2+}$ concentrations correlated with a lower expression of pro-inflammatory factors and a higher expression of anti-inflammatory factors.[33] This is consistent with the results in the present study, validating that PSBP scaffolds have excellent immunomodulatory capabilities.

Micro-computed tomography (micro-CT) is a non-invasive, high-resolution imaging technique that enables clear visualization of the internal microstructure of bone tissue, especially for detecting new bone tissue in small animals.[60,72] To evaluate the *in vivo* bone repair effects of the three scaffold groups, this study established a bilateral cranial bone defect model in SD rats. SD rats were chosen for their low cost and size, which is suitable for surgical manipulation.[73,74] Micro-CT was used to observe new bone growth in the bone defect area. The bone repair effect was then microscopically evaluated using quantitative indexes, such as bone mineral density and bone volume fraction.[75] The micro-CT 3D-reconstructed images highlighted that the PSBP scaffolds—as bone defect-filling materials—exhibited significant new bone growth (Figure 11A). Likewise, the bone volume fraction and bone density analysis results were consistent with the micro-CT results (Figure 11B and C), further validating that PSBP scaffolds have better bone repair effects compared to the other scaffolds. In addition, HE staining, a commonly used method to observe tissue growth, was performed on rat cranial specimens from all scaffold groups to observe bone tissue structure.[76] The HE staining results revealed that at postoperative months 1, 2, and 3, the PSBP scaffold group had more bone tissue formation than the SBP, P, and blank scaffold groups (Figure 12). Masson staining results also indicated that the PSBP scaffold group exhibited better osteogenesis (Figure 13).

The immunomodulatory capacity of implanted scaffolds is important in promoting osteogenic differentiation and angiogenesis.[77] To further assess the immunomodulation and bone repair effects of each scaffold group, immunofluorescence staining was used to analyze cranial defect repair in rats. Generally, iNOS and CD163 are used as polarization markers for M1 and M2 MPs, respectively.[78,79] It has been reported that PDA reduces the expression of M1 MP markers by scavenging ROS[80,81] and that $Sr^{2+}$ activates the PI3K/AKT/mTOR pathway to promote M2 MP polarization.[66] In this study, the immunofluorescence staining results demonstrated that the PSBP scaffolds significantly upregulated the expression of the M2 MP marker CD163 and downregulated the expression of the M1 MP marker iNOS (Figure 14). This suggests that the PSBP scaffolds promoted MP polarization of M1 MPs to M2 MPs, resulting in more M2 MPs in the immune microenvironment. This polarization attenuated the inflammatory response in the early stage of bone repair and promoted bone defect repair.[82,83] In addition, more M2 MPs contributed to osteogenesis on the scaffold surface, ultimately leading to good osseointegration.[84] Therefore, PSBP scaffolds have good immunomodulatory properties, and PDA, together with $Sr^{2+}$, promotes MP polarization toward the M2 phenotype. In promoting bone repair, BMP-2, a key osteoinductive growth factor, induces targeted differentiation of undifferentiated BMSCs into osteoblasts and promotes osteoblast differentiation and maturation, thereby accelerating bone defect repair.[85,86] In this study, the PSBP scaffolds expressed higher levels of BMP-2 at the defect site, suggesting a strong osteogenic induction ability. Additionally, vascularization is a key part of the bone repair process and directly affects the repair and remodeling

of bone tissue.[87] VEGF expression is strongly associated with neovascularization,[88] and our immunofluorescence staining results demonstrated that the PSBP scaffolds effectively promoted VEGF expression. This enhancement is attributed to the synergistic pro-angiogenic effects of $Sr^{2+}$ and $Si^{4+}$ released by SrBG.[89] Furthermore, surface modification with PDA further enhanced angiogenesis and maturation of the cell as well as tissue.[90,91]

Overall, the PDA/SrBG/PCL composite scaffolds prepared in this study can better regulate the immune microenvironment, promote blood vessel regeneration, and facilitate bone defect repair. Nonetheless, the study had several limitations, namely the short observation period and the preliminary *in vivo* investigation, thereby warranting further investigation into the mechanism of bone defect repair.

## 5. Conclusion

In this study, a PDA/SrBG/PCL composite scaffold was fabricated, combining the multifunctional properties of material modification, immunomodulation, and osteogenesis induction. Overall, the PDA/SrBG/PCL scaffolds facilitated bone differentiation *in vitro* and bone repair in an *in vivo* cranial defect model. Therefore, the composite scaffold may potentially overcome the clinical limitations of traditional PCL scaffolds and mark a shift from mere structural replacement to functional reconstruction in bone tissue engineering, offering a valuable reference for the future development of advanced bone repair materials.

## Acknowledgments

None.

## Funding

This research was supported by the National Natural Science Foundation of China (82160577, 32000964), the Zunyi City Innovation Team Fund (Zunyi Science Talent [2024] No. 4), Guangdong Province Science and Technology Plan Project (2024A1515012265), and the Hainan Academician Innovation Center (Nanfan Medical Materials and Health Technology Innovation Center) (2022GDASZH-2022020402-01).

## Conflict of interest

The authors declare no financial and personal relationships with other entities or organizations that can inappropriately influence the present work. They also have no professional or other personal interest of any nature or kind with any product, service, and/or company that could be construed as influencing the position presented in, or the review of, the current manuscript.

## Author contributions

*Conceptualization:* Qiping Huang, Xiang Li, Weikang Xu, Qingde Wa
*Data curation:* Qiping Huang, Xiang Li, Qinghong Fan, Qian Du, Guangquan Zhao, Yuanhao Lv, Yixiao Wang, Weikang Xu, Qingde Wa
*Formal analysis:* Qiping Huang, Xiang Li, Qian Du, Guangquan Zhao, Yuanhao Lv, Yixiao Wang
*Funding acquisition:* Weikang Xu, Qingde Wa
*Investigation:* Qiping Huang, Xiang Li
*Methodology:* Qiping Huang, Xiang Li
*Project administration:* Qiping Huang, Xiang Li, Qian Du, Guangquan Zhao, Yuanhao Lv, Yixiao Wang
*Resources:* Qiping Huang, Xiang Li
*Validation:* Weikang Xu, Qingde Wa
*Visualization:* Weikang Xu, Qingde Wa
*Writing – original draft:* Qiping Huang, Xiang Li
*Writing – review and editing:* Weikang Xu, Qingde Wa

## Ethics approval and consent to participate

All animal experiments were performed according to the protocol approved by the Institutional Animal Care and Use Committee of Guangdong Quality Supervision and Testing Station for Medical and Health Care Appliances (Approval ID: ZMU21-2412-019).

## Consent for publication

Not applicable.

## Availability of data

Upon reasonable request, data can be obtained from the corresponding author.

## References

1. Chi J, Wang M, Chen J, et al. Topographic orientation of scaffolds for tissue regeneration: recent advances in biomaterial design and applications. *Biomimetics (Basel).* 2022;7(3):131.
doi: 10.3390/biomimetics7030131

2. Yang X, Wang Y, Zhou Y, et al. The application of polycaprolactone in three-dimensional printing scaffolds for bone tissue engineering. *Polymers (Basel).* 2021;13(16):2754.
doi: 10.3390/polym13162754

3. Mancuso E, Shah L, Jindal S, et al. Additively manufactured BaTiO(3) composite scaffolds: a novel strategy for load bearing bone tissue engineering applications. *Mater Sci Eng C Mater Biol Appl.* 2021;126:112192.
doi: 10.1016/j.msec.2021.112192

4. Gómez-Lizárraga KK, Flores-Morales C, Del Prado-Audelo ML, et al. Polycaprolactone- and polycaprolactone/ceramic-

based 3D-bioplotted porous scaffolds for bone regeneration: a comparative study. *Mater Sci Eng C Mater Biol Appl*. 2017;79:326-335.
doi: 10.1016/j.msec.2017.05.003

5. Zhao QM, Sun YY, Wu CS, et al. Enhanced osteogenic activity and antibacterial ability of manganese-titanium dioxide microporous coating on titanium surfaces. *Nanotoxicology*. 2020;14(3):289-309.
doi: 10.1080/17435390.2019.1690065

6. Zurita-Méndez NN, Carbajal-De la Torre G, Flores-Merino MV, Espinosa-Medina MA. Development of bioactive glass-collagen-hyaluronic acid-polycaprolactone scaffolds for tissue engineering applications. *Front Bioeng Biotechnol*. 2022;10:825903.
doi: 10.3389/fbioe.2022.825903

7. Tian B, Wang N, Jiang Q, et al. The immunogenic reaction and bone defect repair function of ε-poly-L-lysine (EPL)-coated nanoscale PCL/HA scaffold in rabbit calvarial bone defect. *J Mater Sci Mater Med*. 2021;32(6):63.
doi: 10.1007/s10856-021-06533-7

8. Blum C, Taskin MB, Shan J, et al. Appreciating the first line of the human innate immune defense: a strategy to model and alleviate the neutrophil elastase-mediated attack toward bioactivated biomaterials. *Small*. 2021;17(13):e2007551.
doi: 10.1002/smll.202007551

9. Moore EM, Maestas DR, Jr., Cherry CC, et al. Biomaterials direct functional B cell response in a material-specific manner. *Sci Adv*. 2021;7(49):eabj5830.
doi: 10.1126/sciadv.abj5830

10. Knecht RS, Bucher CH, Van Linthout S, et al. Mechanobiological principles influence the immune response in regeneration: implications for bone healing. *Front Bioeng Biotechnol*. 2021;9:614508.
doi: 10.3389/fbioe.2021.614508

11. Zhang B, Su Y, Zhou J, et al. Toward a better regeneration through implant-mediated immunomodulation: harnessing the immune responses. *Adv Sci (Weinh)*. 2021;8(16):e2100446.
doi: 10.1002/advs.202100446

12. Ben Letaifa R, Klaylat T, Tarchala M, et al. Osteoimmunology: an overview of the interplay of the immune system and the bone tissue in fracture healing. *Surgeries*. 2024;5(2):402-414.
doi: 10.3390/surgeries5020033

13. Jiang F, Zhao H, Zhang P, et al. Challenges in tendon-bone healing: emphasizing inflammatory modulation mechanisms and treatment. *Front Endocrinol (Lausanne)*. 2024;15:1485876.
doi: 10.3389/fendo.2024.1485876

14. Sadowska JM, Ginebra MP. Inflammation and biomaterials: role of the immune response in bone regeneration by inorganic scaffolds. *J Mater Chem B*. 2020;8(41):9404-9427.
doi: 10.1039/d0tb01379j

15. Wei S, Wang Y, Sun Y, *et al*. Biodegradable silk fibroin scaffold doped with mineralized collagen induces bone regeneration in rat cranial defects. *Int J Biol Macromol*. 2023;235:123861.
doi: 10.1016/j.ijbiomac.2023.123861

16. Kawcher Alam M, Sahadat Hossain M, Anisur Rahman Dayan M, *et al*. Fabrication and characterization of a bioscaffold using hydroxyapatite and unsaturated polyester resin. *ACS Omega*. 2024;9(13):15210-15221.
doi: 10.1021/acsomega.3c09599

17. Ye B, Wu B, Su Y, et al. Recent advances in the application of natural and synthetic polymer-based scaffolds in musculoskeletal regeneration. *Polymers (Basel)*. 2022;14(21):4566.
doi: 10.3390/polym14214566

18. Dong C, Tan G, Zhang G, et al. The function of immunomodulation and biomaterials for scaffold in the process of bone defect repair: a review. *Front Bioeng Biotechnol*. 2023;11:1133995.
doi: 10.3389/fbioe.2023.1133995

19. Handley EL, Callanan A. Effects of electrospun fibers containing ascorbic acid on oxidative stress reduction for cardiac tissue engineering. *J Appl Polym Sci*. 2023;140(32):e54242.
doi: 10.1002/app.54242

20. Homaeigohar S, Boccaccini AR. Nature-derived and synthetic additives to poly(ε-caprolactone) nanofibrous systems for biomedicine; an updated overview. *Front Chem*. 2021;9:809676.
doi: 10.3389/fchem.2021.809676

21. Gniesmer S, Brehm R, Hoffmann A, et al. In vivo analysis of vascularization and biocompatibility of electrospun polycaprolactone fibre mats in the rat femur chamber. *J Tissue Eng Regen Med*. 2019;13(7):1190-1202.
doi: 10.1002/term.2868

22. Han Y, Jia B, Lian M, et al. High-precision, gelatin-based, hybrid, bilayer scaffolds using melt electro-writing to repair cartilage injury. *Bioact Mater*. 2021;6(7):2173-2186.
doi: 10.1016/j.bioactmat.2020.12.018

23. Zhao S, Xie K, Guo Y, et al. Fabrication and biological activity of 3D-printed polycaprolactone/magnesium porous scaffolds for critical size bone defect repair. *ACS Biomater Sci Eng*. 2020;6(9):5120-5131.
doi: 10.1021/acsbiomaterials.9b01911

24. Tang C, Shen Y, Xing Y, et al. 3D-printed stents loaded with *Panax notoginseng* saponin for promoting re-endothelialization and reducing local inflammation in the carotid artery of rabbits. *ACS Biomater Sci Eng*. 2024;10(10):6483-6497.
doi: 10.1021/acsbiomaterials.4c00925

25. Liu J, Du G, Yu H, et al. Synthesis of hierarchically porous bioactive glass and its mineralization activity. *Molecules*. 2023;28(5):2224.
doi: 10.3390/molecules28052224

26. Liang J, Lu X, Zheng X, et al. Modification of titanium orthopedic implants with bioactive glass: a systematic review of in vivo and in vitro studies. *Front Bioeng Biotechnol.* 2023; 11:1269223.
doi: 10.3389/fbioe.2023.1269223

27. Zhao H, Wang X, Jin A, et al. Reducing relapse and accelerating osteogenesis in rapid maxillary expansion using an injectable mesoporous bioactive glass/fibrin glue composite hydrogel. *Bioact Mater*. 2022;18:507-525.
doi: 10.1016/j.bioactmat.2022.03.001

28. Oliver JN, Su Y, Lu X, et al. Bioactive glass coatings on metallic implants for biomedical applications. *Bioact Mater*. 2019;4:261-270.
doi: 10.1016/j.bioactmat.2019.09.002

29. Chakraborty A, Bodhak S, Tah I, et al. Tailored bioactive glass coating: navigating devitrification toward a superior implant performance. *ACS Biomater Sci Eng*. 2024;10(8): 5300-5312.
doi: 10.1021/acsbiomaterials.4c01032

30. Wa Q, Luo Y, Tang Y, et al. Mesoporous bioactive glass-enhanced MSC-derived exosomes promote bone regeneration and immunomodulation in vitro and in vivo. *J Orthop Translat*. 2024;49:264-282.
doi: 10.1016/j.jot.2024.09.009

31. Lin K, Wang X, Zhang N, Shen Y. Strontium (Sr) strengthens the silicon (Si) upon osteoblast proliferation, osteogenic differentiation and angiogenic factor expression. *J Mater Chem B*. 2016;4(21):3632-3638.
doi: 10.1039/c6tb00735j

32. Liu X, Huang H, Zhang J, et al. Recent advance of strontium functionalized in biomaterials for bone regeneration. *Bioengineering (Basel)*. 2023;10(4):414.
doi: 10.3390/bioengineering10040414

33. Zhao F, Lei B, Li X, et al. Promoting in vivo early angiogenesis with sub-micrometer strontium-contained bioactive microspheres through modulating macrophage phenotypes. *Biomaterials*. 2018;178:36-47.
doi: 10.1016/j.biomaterials.2018.06.004

34. Ding J, Zhao J, Wang L, et al. Regulated contribution of local and systemic immunity to new bone regeneration by modulating B/Sr concentration of bioactive borosilicate glass. *Mater Today Bio*. 2023;19:100585.
doi: 10.1016/j.mtbio.2023.100585

35. Li M, Wang M, Wen Y, et al. Signaling pathways in macrophages: molecular mechanisms and therapeutic targets. *MedComm. (2020)*. 2023;4(5):e349.
doi: 10.1002/mco2.349

36. Terzopoulou Z, Baciu D, Gounari E, et al. Composite membranes of poly(ε-caprolactone) with bisphosphonate-loaded bioactive glasses for potential bone tissue engineering applications. *Molecules*. 2019;24(17):3067.
doi: 10.3390/molecules24173067

37. Sheng X, Li C, Wang Z, et al. Advanced applications of strontium-containing biomaterials in bone tissue engineering. *Mater Today Bio*. 2023;20:100636.
doi: 10.1016/j.mtbio.2023.100636

38. Poh PS, Hutmacher DW, Stevens MM, Woodruff MA. Fabrication and in vitro characterization of bioactive glass composite scaffolds for bone regeneration. *Biofabrication*. 2013;5(4):045005.
doi: 10.1088/1758-5082/5/4/045005

39. Ma T, Wang CX, Ge XY, Zhang Y. Applications of polydopamine in implant surface modification. *Macromol Biosci*. 2023;23(10):e2300067.
doi: 10.1002/mabi.202300067

40. Qin D, Zhao Y, Cheng R, et al. Mussel-inspired immunomodulatory and osteoinductive dual-functional hydroxyapatite nanoplatform for promoting bone regeneration. *J Nanobiotechnology*. 2024;22(1):320.
doi: 10.1186/s12951-024-02593-3

41. Jin L, Yuan F, Chen C, et al. Degradation products of polydopamine restrained inflammatory response of LPS-stimulated macrophages through mediation TLR-4-MYD88 dependent signaling pathways by antioxidant. *Inflammation*. 2019;42(2):658-671.
doi: 10.1007/s10753-018-0923-3

42. Park J, Lee SJ, Jung TG, et al. Surface modification of a three-dimensional polycaprolactone scaffold by polydopamine, biomineralization, and BMP-2 immobilization for potential bone tissue applications. *Colloids Surf B Biointerfaces*. 2021;199:111528.
doi: 10.1016/j.colsurfb.2020.111528

43. Ye G, Bao F, Zhang X, et al. Nanomaterial-based scaffolds for bone tissue engineering and regeneration. *Nanomedicine (Lond)*. 2020;15(20):1995-2017.
doi: 10.2217/nnm-2020-0112

44. Bharadwaz A, Jayasuriya AC. Recent trends in the application of widely used natural and synthetic polymer nanocomposites in bone tissue regeneration. *Mater Sci Eng C Mater Biol Appl*. 2020;110:110698.
doi: 10.1016/j.msec.2020.110698

45. Fazeli N, Arefian E, Irani S, et al. 3D-printed PCL scaffolds coated with nanobioceramics enhance osteogenic differentiation of stem cells. *ACS Omega*. 2021;6(51): 35284-35296.
doi: 10.1021/acsomega.1c04015

46. Abd El-Hamid HK, El-Kheshen AA, Abdou AM, Elwan RL. Incorporation of strontium borosilicate bioactive glass in calcium aluminate biocement: physicomechanical, bioactivity and antimicrobial properties. *J Mech Behav Biomed Mater*. 2023;144:105976.
doi: 10.1016/j.jmbbm.2023.105976

47. Zhao Q, Gao S. Poly (butylene succinate)/silicon nitride nanocomposite with optimized physicochemical properties,

biocompatibility, degradability, and osteogenesis for cranial bone repair. *J Funct Biomater.* 2022;13(4):231. doi: 10.3390/jfb13040231

48. Wu Y, Liu J, Kang L, et al. An overview of 3D printed metal implants in orthopedic applications: present and future perspectives. Heliyon. 2023;9(7):e17718. doi: 10.1016/j.heliyon.2023.e17718

49. Zhang L, Yang G, Johnson BN, Jia X. Three-dimensional (3D) printed scaffold and material selection for bone repair. *Acta Biomater.* 2019;84:16-33. doi: 10.1016/j.actbio.2018.11.039

50. Toosi S, Javid-Naderi MJ, Tamayol A, et al. Additively manufactured porous scaffolds by design for treatment of bone defects. *Front Bioeng Biotechnol.* 2023;11:1252636. doi: 10.3389/fbioe.2023.1252636

51. Bouakaz I, Drouet C, Grossin D, et al. Hydroxyapatite 3D-printed scaffolds with gyroid-triply periodic minimal surface porous structure: fabrication and an in vivo pilot study in sheep. *Acta Biomater.* 2023;170:580-595. doi: 10.1016/j.actbio.2023.08.041

52. Du J, Zhou Y, Bao X, et al. Surface polydopamine modification of bone defect repair materials: characteristics and applications. *Front Bioeng Biotechnol.* 2022;10:974533. doi: 10.3389/fbioe.2022.974533

53. Ghalia MA, Alhanish A. Mechanical and biodegradability of porous PCL/PEG copolymer-reinforced cellulose nanofibers for soft tissue engineering applications. *Med Eng Phys.* 2023;120:104055. doi: 10.1016/j.medengphy.2023.104055

54. Xiao L, Li Y, Geng R, et al. Polymer composite microspheres loading (177)Lu radionuclide for interventional radioembolization therapy and real-time SPECT imaging of hepatic cancer. *Biomater Res.* 2023;27(1):110. doi: 10.1186/s40824-023-00455-x

55. Mahnavi A, Shahriari-Khalaji M, Hosseinpour B, et al. Evaluation of cell adhesion and osteoconductivity in bone substitutes modified by polydopamine. *Front Bioeng Biotechnol.* 2022;10:1057699. doi: 10.3389/fbioe.2022.1057699

56. Wang H, Yuan C, Lin K, et al. Modifying a 3D-printed Ti6Al4V implant with polydopamine coating to improve BMSCs growth, osteogenic differentiation, and in situ osseointegration in vivo. *Front Bioeng Biotechnol.* 2021;9:761911. doi: 10.3389/fbioe.2021.761911

57. Zhao ZH, Ma XL, Ma JX, et al. Sustained release of naringin from silk-fibroin-nanohydroxyapatite scaffold for the enhancement of bone regeneration. *Mater Today Bio.* 2022;13:100206. doi: 10.1016/j.mtbio.2022.100206

58. Devi VK A, Ray S, Arora U, et al. Dual drug delivery platforms for bone tissue engineering. *Front Bioeng Biotechnol.* 2022;10:969843. doi: 10.3389/fbioe.2022.969843

59. S S, R G AP, Bajaj G, et al. A review on the recent applications of synthetic biopolymers in 3D printing for biomedical applications. *J Mater Sci Mater Med.* 2023;34(12):62. doi: 10.1007/s10856-023-06765-9

60. Wang S, Gu R, Wang F, et al. 3D-Printed PCL/Zn scaffolds for bone regeneration with a dose-dependent effect on osteogenesis and osteoclastogenesis. *Mater Today Bio.* 2022;13:100202. doi: 10.1016/j.mtbio.2021.100202

61. Murugan S, Parcha SR. Fabrication techniques involved in developing the composite scaffolds PCL/HA nanoparticles for bone tissue engineering applications. *J Mater Sci Mater Med.* 2021;32(8):93. doi: 10.1007/s10856-021-06564-0

62. Labbaf S, Tsigkou O, Müller KH, et al. Spherical bioactive glass particles and their interaction with human mesenchymal stem cells in vitro. *Biomaterials.* 2011;32(4): 1010-1018. doi: 10.1016/j.biomaterials.2010.08.082

63. Ma YX, Jiao K, Wan QQ, et al. Silicified collagen scaffold induces semaphorin 3A secretion by sensory nerves to improve in-situ bone regeneration. *Bioact Mater.* 2022;9: 475-490. doi: 10.1016/j.bioactmat.2021.07.016

64. Qiu P, Li M, Chen K, et al. Periosteal matrix-derived hydrogel promotes bone repair through an early immune regulation coupled with enhanced angio- and osteogenesis. *Biomaterials.* 2020;227:119552. doi: 10.1016/j.biomaterials.2019.119552

65. Zhang Y, Yu W, Ba Z, et al. 3D-printed scaffolds of mesoporous bioglass/gliadin/polycaprolactone ternary composite for enhancement of compressive strength, degradability, cell responses and new bone tissue ingrowth. *Int J Nanomed.* 2018;13:5433-5447. doi: 10.2147/ijn.S164869

66. Qiu H, Xiong H, Zheng J, et al. Sr-incorporated bioactive glass remodels the immunological microenvironment by enhancing the mitochondrial function of macrophage via the PI3K/AKT/mTOR signaling pathway. *ACS Biomater Sci Eng.* 2024;10(6):3923-3934. doi: 10.1021/acsbiomaterials.4c00228

67. Ajita J, Saravanan S, Selvamurugan N. Effect of size of bioactive glass nanoparticles on mesenchymal stem cell proliferation for dental and orthopedic applications. *Mater Sci Eng C Mater Biol Appl.* 2015;53:142-149. doi: 10.1016/j.msec.2015.04.041

68. Feito MJ, Casarrubios L, Oñaderra M, et al. Response of RAW 264.7 and J774A.1 macrophages to particles and nanoparticles of a mesoporous bioactive glass: a comparative study. *Colloids Surf B Biointerfaces*. 2021;208:112110. doi: 10.1016/j.colsurfb.2021.112110

69. Xu H, Zhu Y, Hsiao AW, et al. Bioactive glass-elicited stem cell-derived extracellular vesicles regulate M2 macrophage polarization and angiogenesis to improve tendon regeneration and functional recovery. *Biomaterials*. 2023;294:121998. doi: 10.1016/j.biomaterials.2023.121998

70. Römer P, Desaga B, Proff P, et al. Strontium promotes cell proliferation and suppresses IL-6 expression in human PDL cells. *Ann Anat*. 2012;194(2):208-211. doi: 10.1016/j.aanat.2011.09.008

71. Buache E, Velard F, Bauden E, et al. Effect of strontium-substituted biphasic calcium phosphate on inflammatory mediators production by human monocytes. *Acta Biomater*. 2012;8(8):3113-3119. doi: 10.1016/j.actbio.2012.04.045

72. Palczewska-Komsa MP, Gapiński B, Nowicka A. The influence of new bioactive materials on pulp-dentin complex regeneration in the assessment of cone bone computed tomography (CBCT) and computed micro-tomography (Micro-CT) from a present and future perspective-a systematic review. *J Clin Med*. 2022;11(11):3091. doi: 10.3390/jcm11113091

73. Mohan S, Karunanithi P, Raman Murali M, et al. Potential use of 3D CORAGRAF-loaded PDGF-BB in PLGA microsphere seeded mesenchymal stromal cells in enhancing the repair of calvaria critical-size bone defect in rat model. *Mar Drugs*. 2022;20(9):561. doi: 10.3390/md20090561

74. Lee JB, Seo MS. Mandibular incisors with two canals are associated with the presence of the distolingual root in mandibular first molars: a cone-beam computed tomographic study. BMC Oral Health. 2022;22(1):145. doi: 10.1186/s12903-022-02184-4

75. Song W, Zhao L, Gao Y, et al. Dual growth factor-modified microspheres nesting human-derived umbilical cord mesenchymal stem cells for bone regeneration. *J Biol Eng*. 2023;17(1):43. doi: 10.1186/s13036-023-00360-w

76. Wang C, Wu J, Liu L, et al. Improving osteoinduction and osteogenesis of Ti6Al4V alloy porous scaffold by regulating the pore structure. *Front Chem*. 2023;11:1190630. doi: 10.3389/fchem.2023.1190630

77. Okizaki S, Ito Y, Hosono K, et al. Suppressed recruitment of alternatively activated macrophages reduces TGF-β1 and impairs wound healing in streptozotocin-induced diabetic mice. *Biomed Pharmacother*. 2015;70:317-325. doi: 10.1016/j.biopha.2014.10.020

78. Zhu C, Kros JM, van der Weiden M, et al. Expression site of P2RY12 in residential microglial cells in astrocytomas correlates with M1 and M2 marker expression and tumor grade. *Acta Neuropathol Commun*. 2017;5(1):4. doi: 10.1186/s40478-016-0405-5

79. Lisi L, Ciotti GM, Braun D, et al. Expression of iNOS, CD163 and ARG-1 taken as M1 and M2 markers of microglial polarization in human glioblastoma and the surrounding normal parenchyma. *Neurosci Lett*. 2017;645:106-112. doi: 10.1016/j.neulet.2017.02.076

80. Wu S, Dong R, Xie Y, et al. CO-loaded hemoglobin/EGCG nanoparticles functional coatings for inflammation modulation of vascular implants. *Regen Biomater*. 2025;12:rbae148. doi: 10.1093/rb/rbae148

81. Luo R, Su J, Zhang W, et al. Targeted delivery of NO donor and ROS scavenger for synergistic treatment of rheumatoid arthritis. *Biomed Pharmacother*. 2024;174:116540. doi: 10.1016/j.biopha.2024.116540

82. Chen X, Wang M, Chen F, et al. Correlations between macrophage polarization and osteoinduction of porous calcium phosphate ceramics. *Acta Biomater*. 2020;103:318-332. doi: 10.1016/j.actbio.2019.12.019

83. Alhamdi JR, Peng T, Al-Naggar IM, et al. Controlled M1-to-M2 transition of aged macrophages by calcium phosphate coatings. *Biomaterials*. 2019;196:90-99. doi: 10.1016/j.biomaterials.2018.07.012

84. Ye J, Xie C, Wang C, et al. Promoting musculoskeletal system soft tissue regeneration by biomaterial-mediated modulation of macrophage polarization. *Bioact Mater*. 2021;6(11):4096-4109. doi: 10.1016/j.bioactmat.2021.04.017

85. Gélébart P, Cuenot S, Sinquin C, et al. Microgels based on Infernan, a glycosaminoglycan-mimetic bacterial exopolysaccharide, as BMP-2 delivery systems. *Carbohydr Polym*. 2022;284:119191. doi: 10.1016/j.carbpol.2022.119191

86. Kathami N, Moreno-Vicente C, Martín P, et al. rhBMP-2 induces terminal differentiation of human bone marrow mesenchymal stromal cells only by synergizing with other signals. *Stem Cell Res Ther*. 2024;15(1):124. doi: 10.1186/s13287-024-03735-y

87. Li T, Peng M, Yang Z, et al. 3D-printed IFN-γ-loading calcium silicate-β-tricalcium phosphate scaffold sequentially activates M1 and M2 polarization of macrophages to promote vascularization of tissue engineering bone. *Acta Biomater*. 2018;71:96-107. doi: 10.1016/j.actbio.2018.03.012

88. Liu Y, Li Z, Li W, et al. Discovery of β-sitosterol's effects on molecular changes in rat diabetic wounds and its impact on angiogenesis and macrophages. *Int Immunopharmacol*. 2024;126:111283.

doi: 10.1016/j.intimp.2023.111283

89. Mao L, Xia L, Chang J, et al. The synergistic effects of Sr and Si bioactive ions on osteogenesis, osteoclastogenesis and angiogenesis for osteoporotic bone regeneration. *Acta Biomater*. 2017;61:217-232.
doi: 10.1016/j.actbio.2017.08.015

90. Zhu X, Wu S, Yang K, et al. Polydopamine-modified konjac glucomannan scaffold with sustained release of vascular endothelial growth factor to promote angiogenesis. *Int J Biol Macromol*. 2024;271(Pt 1):132333.
doi: 10.1016/j.ijbiomac.2024.132333

91. Cheng S, Wang D, Ke J, et al. Improved in vitro angiogenic behavior of human umbilical vein endothelial cells with oxidized polydopamine coating. *Colloids Surf B Biointerfaces*. 2020;194:111176.
doi: 10.1016/j.colsurfb.2020.111176

## Appendix

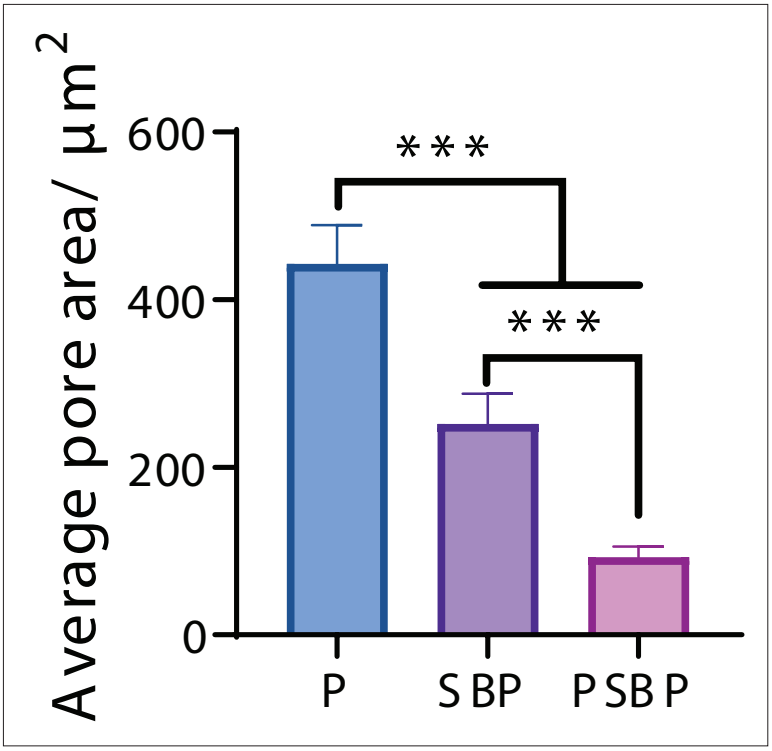


**Figure A1**. Pore area on the fibers of three groups of scaffolds ($n = 6$; ***$p < 0.001$). Abbreviations: P, polycaprolactone (PCL); PSBP, polydopamine (PDA)/strontium (Sr)-doped bioactive glass (SrBG)/polycaprolactone (PCL); SBP, strontium (Sr)-doped bioactive glass (SrBG)/polycaprolactone (PCL).